POLITECNICO DI MILANO

School of Industrial and Information Engineering

Master degree in Materials Engineering and Nanotechnology

Control and stability of electrical and optical properties of nanostructured Al:ZnO transparent conducting layers

Supervisor: **Ing. Andrea LI BASSI**

Assistant Supervisor: **Ing. Paolo Gondoni**

Matteo SCOLARO

Matr. 778014

Academic Year 2012-2013

Contents

List of figures

List of tables

Abstract

A continuous effort in researching new materials and technologies in the photovoltaic field verges to nanostructured devices. The research of Transparent Conducting Oxides (TCO) draws the attention to materials which contribute to break down costs and environmental impact, as Aluminum doped Zinc Oxide. In this thesis work AZO thin films, deposited with Pulsed Laser Deposition (PLD) at a pressure of 110 Pa, show hierarchical tree-like nanostructures which allow high light trapping ability and light transmission in contrast with poor electrical conductivity. The use of mixed deposition atmospheres of Ar:O_2 , with different O_2 partial pressure combinations, permits to study the contribution of oxygen vacancies to material functional properties. In particular morphology analysis is carried on with a scanning electron microscope; electrical and optical properties, as resistivity, carrier density, Hall mobility, optical transmittance and haze factor, are measured and discussed with respect to O_2 partial pressure variation. It is demonstrated that a reduction of this parameter until 2.5% confers to AZO the most optimal combination of functional properties considered: electrical resistivity of $3.17 \cdot 10^{-1}$ Ω cm, a transmittance in the visible range of 66.5% and a haze factor of 96.5%. Beyond these important properties, a qualitative study about degradation of thin films is performed. After the deposition, nanostructured films and also one film with a columnar compact structure (deposited at a pressure of 2 Pa in O_2 atmosphere) were monitored with electrical measurements for one month. These measurements and in addition optical transmittance measurements were also performed on samples deposed about 3 years ago at a pressure between 0.01 and 10 Pa in O_2 atmosphere, with a compact columnar structure. The effect of ageing degradation is heavily present in nanostructured films, while compact films do not suffer significant variation; this is probably due to their lower porosity, which is a critical parameter for diffusion and segregation of chemical species at grain boundaries or surface.

Sommario

Uno sforzo continuo nella ricerca di nuovi materiali e tecnologie nell'ambito del fotovoltaico, protende verso l'applicazione di dispositivi nanostrutturati. La ricerca di ossidi trasparenti conduttori(TCO) richiama l'attenzione verso materiali che contribuiscono ad abbattere sia i costi che l'impatto con l'ambiente, come l'ossido di zinco drogato con alluminio (AZO). In questo lavoro di tesi film sottili di AZO, fabbricati con la tecnica di ablazione laser pulsata (PLD) con una pressione di 110 Pa, mostrano nanostrutture gerarchiche a forma di alberi, che consentono elevate capacità di intrappolamento e trasmissione della radiazione luminosa, in contrasto con una scarsa conduttività elettrica. L'uso di una miscela di Ar:O_2 come atmosfera di deposizione, con diverse combinazioni di pressione parziale di O_2, consente di studiare il contributo delle vacanze di ossigeno in alcune proprietà funzionali. In particolare viene effettuata un'analisi della morfologia e della struttura con un microscopio elettronico a scansione (SEM), mentre alcune proprietà elettriche e ottiche, come la resistività, densità di carica, mobilità di Hall, trasmittanza e haze factor, vengono misurate e discusse rispetto alla variazione di pressione parziale di O_2. Si dimostra che una riduzione di tale parametro fino al 2,5%, conferisce all'AZO la combinazione più ottimale di proprietà funzionali considerate: una resistività elettrica di $3.17 \cdot 10^{-1}$ Ω cm, una trasmittanza nel visibile del 66.5% e un haze factor del 96.5%. Al di là di queste importanti caratteristiche, viene eseguito uno studio qualitativo sulla degradazione per invecchiamento dei film sottili. Immediatamente dopo la deposizione, i film nanostrutturati e, in aggiunta, un film con una struttura colonnare compatta (deposto ad una pressione di 2 Pa in atmosfera di ossigeno) sono stati monitorati con misurazioni elettriche per un mese circa. Tali misure, con in aggiunta la misura di trasmittanza ottica, sono state eseguite anche su campioni deposti circa 3 anni fa ad una pressione tra 0,01 e 10 Pa in atmosfera di O_2 , con una struttura colonnare compatta. L'effetto della degradazione sulle proprietà analizzate è fortemente presente in film nanostrutturati, mentre i film compatti non subiscono variazioni

significative; ciò probabilmente avviene a causa della loro minor porosità, la quale risulta essere un parametro fondamentale per la diffusione e la segregazione di specie chimiche nei bordi grano dei film.

Introduction

The main arguments of this thesis work is the study of the influence of O_2 vacancies on functional properties of nanostructured thin film of Aluminum doped Zinc Oxide, moreover the effects of ageing degradation on these properties were observed.

The desire of reducing the emission of pollutants and of removing the dependence on energy production using fossil fuels, leads us towards the search for new sources of clean energy. This pursuit presents different obstacles from the economic and applicative point of view and photovoltaic is one of main solutions and research topic. The requirement of increasing the efficiency and durability of solar cells always involves a greater effort in the optimization of single components of such devices.

The research on Transparent Conducting Oxide (TCO) converge in this direction. They are an essential part of this technology, commonly used as electrode or photoanode in thin film and 3rd generation solar cells. TCOs require high transparency and light scattering ability combined with electrical conductivity. These prerogatives are achieved by means of wide band-gap oxide with strong extrinsic doping process.

One of the most used TCO is Indium Tin Oxide (ITO), which reaches the most performant combination of functional properties. However its costs, due to the shortage on Earth's crust, and its polluting production force to search for other materials. Aluminum doped Zinc Oxide (AZO or Al:ZnO) is one of the most hopeful choice, beacause it is relatively cheap and it has abundant spread in nature.

AZO thin films are widely investigated and many documents are found in literature, mostly for what concerns the influence of dopant and oxygen vacancies on its electrical conductivity; one of most innovative branches of research concerns engineering of different nanostructured thin film. Tuning properties at the nano and microscale can open new possibilities and applications, as photoanode, because an increase of surface/volume ratio implies high light scattering ability. Forest-like structure allows a preferential direction ortogonal to the film plane, for charge carrier transport and light trapping. The main issue of this geometry and nano arrangements,

is the very poor conduction. Therefore the improvement of electrical conductivity is the main purpose of this work, which is focused on the influence of oxygen vacancies on electrical transport properies. All samples were obtained with Pulsed Laser deposition (PLD) at room temperature; the variation of the deposition pressure inside the vacuum chamber allows to obtain different thin film morphologies and structures; the hierachical tree-like nanostructure is achieved depositing at pressure higher than 10 Pa. The study of influence of oxygen vacancies was perfomerd using a mixed atmosphere of $Ar:O_2$ at 110 Pa, the variation of O_2 partial pressure affects charge carrier concentration of AZO and related electrical properties as resistivity and Hall mobility. The measurements along the in-plane direction referred to these properties was carried on with Van der Pauw procedure and with the exploitation of Hall effect. Furthermore O_2 partial pressure affects optical properties, whose measurement was performed with a UV-vis-NIR spectrophotometer, in order to obtain transmittance and scattered transmittance, which are importante to estimate light transmission and trapping ability. Of course the variation of atmosphere parameters modifies the morphology and structure of the film, which are investigated with a Scanning Electron Microscope (SEM).

As stated before, one of the main issues of the optimization of all components of a solar system is the durability. Life time of the device considerably influences costs and energy waste of the entire system. In this work a monitoring of electrical resistivity alterations was accomplished and possible phenomena which drive ageing degradation processes are discussed. Finally a method to perform a cross-plane electrical measurement was attempted and different ideas are described in this elaborate, this is important because the anisotropy of the material permits to have different properties depending on the transport direction selected.

The overall experimental work is described and related results are discussed in this elaborate. The structure of the thesis is briefly reassumed starting from Chapter 1, which is dedicated to an introduction to TCOs: their type and different application fields, their processing and especially the description of the main funtional properties

characterized in this work are illustrated. Moreover Aluminum doped Zinc Oxide and previous existing research about it are presented. Chapter 2 describes main instruments and experimental techniques exploited to fabricate and characterize AZO nanostructured thin films. In particular Resistive Thermal Evaporation and Pulsed Laser Deposition, used to deposite electrical metal contacts and AZO respectively, are described underlining main features. Finally experimental set-up and measurements methods are displayed: structural, electrical and optical measurement instruments with related procedures. In Chapter 3 experimental results refferred to morphological, structural, electrical, optical analysis are discussed, in addition a qualitative description about degradation of functional properties and cross-plane resistivity measurements is discussed. A correlation among all properties observed and discussed in the elaborate is fulfilled.

Chapter 1

Introduction to Transparent Conducting Oxides

Over the last decade the field of Transparent Conducting Oxides has had a dramatic increase in interest with an increase in the number of active groups and the diversity of materials and approaches. TCOs are an essential part of technologies that require both large-area electrical contact and optical access in the visible range of the light spectrum. High transparency, combined with useful electrical conductivity, is achieved by selecting a wide-band gap oxide (figure 1.1) that is rendered degenerate through the introduction of intrinsic or extrinsic defects due to doping elements, in table 1.1 some TCO materials and relative doping agents are shown, the most common transparent conducting oxides are based on tin oxide, indium oxide, zinc oxide, cadmium oxide and their combinations.

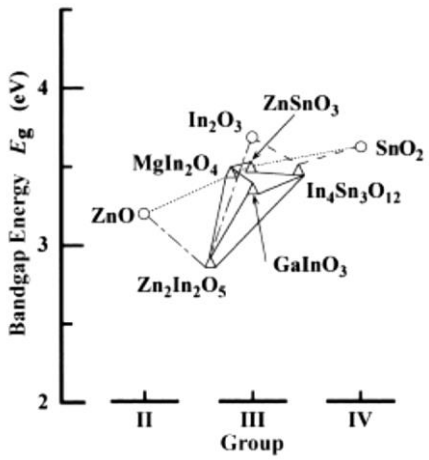

Figure 1.1. Band gap energy of TCO materials: binary (○) and ternary compounds (□) and multicomponent oxides (lines)[1].

TCOs play a critical role in flat-panel monitors, televisions, and other display technologies. Light emitting diodes (LED) and liquid crystal display (LCD) consist of pixels that are turned on and off with application of an electric signal. A transparent conducting oxide layer allows for this signal to be sent to each pixel while remaining transparent to the light produced. ITO ($In:SnO_2$) and IZO (In:ZnO) are widely used in the fabrication of flat-panel display. As the demand for display technologies grows, so will the requirement for high performance TCOs. While they are used to let light out for display application, they are used to allow light in for photovoltaic devices, such application is deeply described in section 1.2. Electrochromic (EC) windows, which darken or become opaque upon application of a certain voltage, an absorber layer is sandwiched between two TCO layers. While the active layer darkens with the applied voltage through the conducting oxide, the oxide must also be highly transparent to visible light when the absorber is not active and functioning as a traditional window. While EC windows are still in a nascent market stage, architectural window glass is a large current market for TCO coatings, typically fluorine-doped tin oxide (SnO_2:F). Since TCOs reflect in the infrared region and absorb in the ultraviolet region, glass can be coated with a TCO to create low-emissivity (low-e) windows that can reduce radiant heat loss and minimize exposure to harmful UV radiation. This can improve the energy efficiency of a building and cut heating and cooling energy costs.

The diverse nature of the materials integrated into these devices, including semiconductors, molecular and polymer organics, ceramics, glass, metal and plastic, have required TCO materials with new performance, processability and even morphology.

Material	Dopant or Compound
SnO_2	Sb, F, As,Nb, Ta
In_2O_3	Sn, Ge,Mo, F, Ti,Zr, Hf,Nb, Ta,W,Te
ZnO	Al,Ga, B, In,Y,Sc, F, V, Si,Ge, Ti,Zr, Hf
CdO	In, Sn
$ZnO–SnO_2$	Zn_2SnO_4, $ZnSnO_3$
$ZnO–In_2O_3$	$Zn_2In_2O_5$, $Zn_3In_2O_6$
$In_2O_3–SnO_2$	$In_4Sn_3O_{12}$
$CdO–SnO_2$	Cd_2SnO_4, $CdSnO_3$
$CdO–In_2O_3$	$CdIn_2O_4$
$MgIn_2O_4$	
$GaInO_3$, $(Ga, In)_2O_3$	Sn,Ge
$CdSb_2O_6$	Y
$ZnO–In_2O_3–SnO_2$	$Zn_2In_2O_5–In_4Sn_3O_{12}$
$CdO–In_2O_3–SnO_2$	$CdIn_2O_4–Cd_2SnO_4$
ZnO–CdO–In2O3–SnO2	

Table 1.1. TCO semiconductors for thin-film transparent electrodes [1].

This has resulted in new n-type materials, the synthesis of p-type materials and novel composite TCO materials as well as an increased set of theoretical and modelling tools for understanding and predicting the behaviour of TCOs, because there is still not a complete theoretical understanding of the materials nor an ability to reliably predict the properties of new materials.

At this point, a brief summary of the relevant optoelectronic properties of conventional TCO materials is provided in section 1.1, to improve the understanding of the physics of this type of material.

1.1 Functional properties

1.1.1 Optical Properties

Optical behaviour of TCOs could be described considering the response to electromagnetic radiation, which include the visible range and both the near infrared and ultraviolet; it implies a transmission window between wavelengths of about 0.4 µm and 1.5 µm.

They exhibit both quantum and classical phenomena. The first prevent light to be transmitted at wavelengths shorter than 0.4 µm, at which absorption occurs due to the fundamental band-gap; the second impede the transmission of light at longer wavelengths, at which reflection occurs because of the plasma edge. The wavelengths at which these transitions occur are determined by a number of fundamental characteristics as well as by the concentration of free electrons.

I proceed discussing the properties of the materials in the near-infrared part of the spectrum. The computation of the optical properties of TCOs in the longer-wavelength region of interest is based on Maxwell's equations and the Drude theory of free electrons [2]. The materials are well described assuming that electrons, delocalized along crystal lattice, do not interact with each other but undergo collisions with ions. Maxwell's equations enable us to define a complex permittivity, composed by real and imaginary parts as follows

$$\varepsilon_1 = \varepsilon_\infty \left(1 - \frac{\omega_p^2}{\omega^2}\right) \tag{1.1}$$

and:

$$\varepsilon_2 = \varepsilon_\infty \left(\frac{\varepsilon_\infty \omega_p^2}{\omega^3 \tau}\right) \tag{1.2}$$

These assume that the electrons are completely free and that $\frac{1}{\tau} << \omega$, where τ is the relaxation time and ω is the frequency of the electric field. The quantity ω_p is known as the *plasma frequency* and is given by:

$$\omega_p = \left(\frac{ne^2}{\varepsilon_0 \varepsilon_\infty m_c^*}\right)^{\frac{1}{2}} \tag{1.3}$$

where *n* is the carrier concentration, *e* is the electronic charge, ε_0 is the permittivity of free space, ε_∞ is the high-frequency permittivity which is defined as the permittivity in the visible range by the Lyddane-Sachs-Teller relation [43] , and m_c^* is the conduction band effective mass. At this frequency, $\varepsilon_1 = 0$, making the properties of the material change dramatically. ω_p is the frequency at which the electron ensemble resonates with the alternating electric field. At higher or lower frequencies, the electrons either lag or lead the electric field. Equation 1 shows that ε_1 is large and negative for $\omega < \omega_p$, but approaches ε_∞ when $\omega > \omega_p$. On the other hand, ε_2 is large and positive for $\omega < \omega_p$, but tends to zero for $\omega > \omega_p$. The real and imaginary parts of the complex refractive index may be derived from Equations 1 and 2. They are

$$N = \sqrt{\frac{1}{2}(\varepsilon_1^2 + \varepsilon_2^2)^{\frac{1}{2}} + \frac{\varepsilon_1}{2}} \tag{1.4}$$

Which is the refractive index, and

$$k' = \sqrt{\frac{1}{2}(\varepsilon_1^2 + \varepsilon_2^2)^{\frac{1}{2}} - \frac{\varepsilon_1}{2}} \tag{1.5}$$

which is the extinction coefficient. At high frequencies, the TCOs behave like a perfect dielectric, whereas at low frequencies $\omega < \omega_p$, at which both *N* and *k*' are large, the material has near-unity reflectance.

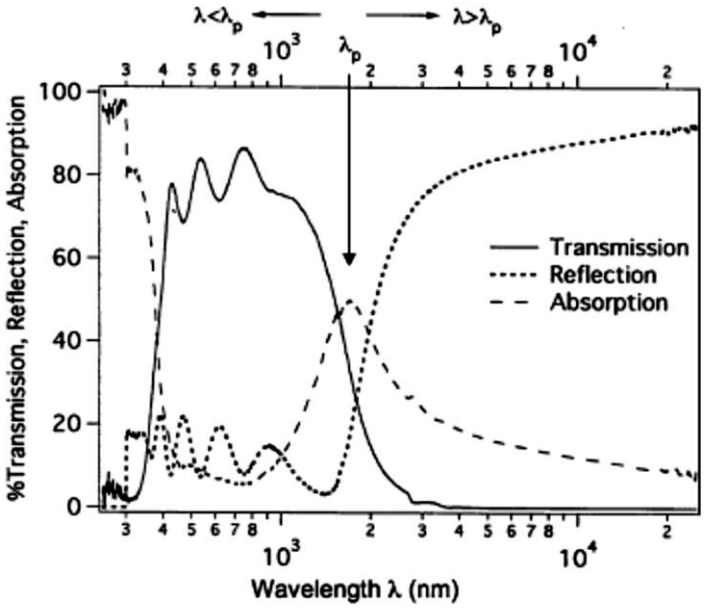

Figure 1.2. Transmission, reflection, and absorption spectra of a typical TCO [3].

Considering a thin film, the visible range of wavelengths is characterized by interference fringes (figure 1.2), which change with film thickness and its refractive index, and a mean reflectance of about 15%. Above the plasma wavelength, the films are characterized by a high reflectance, reaching approximately 90%. The films with lower carrier concentration do not exhibit the increase in reflectance characteristic of the plasma wavelength. As the carrier concentration increase, the height of the free-carrier absorption band increases because there are more carriers to absorb photons, and the width of the peak decreased (figure 1.3).

At very high electron concentrations, this can even decrease the visible wavelength transparency [4].

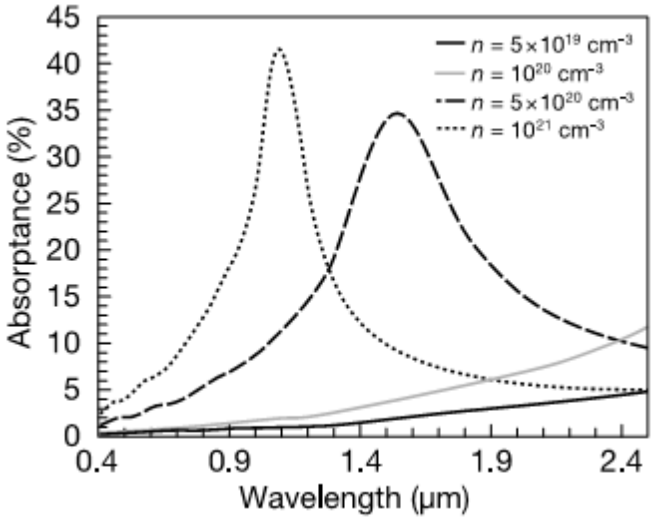

Figure 1.3. Free carrier absorbance of a thin films [5].

Now I consider the visible–near-ultraviolet region, from which additional information may be learned. The fundamental band-gap of these materials is large, often about 3.5–4 eV, which corresponds to a wavelength range of 0.3– 0.35 μm. In the previous discussion, we did not consider absorption due to band to band transitions, and in reality, a typical absorption curve shows a strong increase in the short-wavelength range. For TCOs, the band-to-band transitions are affected by the concentration of free carriers because the materials are degenerate. In nominally doped semiconductors, the Fermi level lies between the conduction and valence bands. As the doping concentration is increased, electrons populate states within the conduction band which pushes the Fermi level higher in energy and in the case of degenerate level of doping, the Fermi level lies inside the conduction band as in figure 1.4.

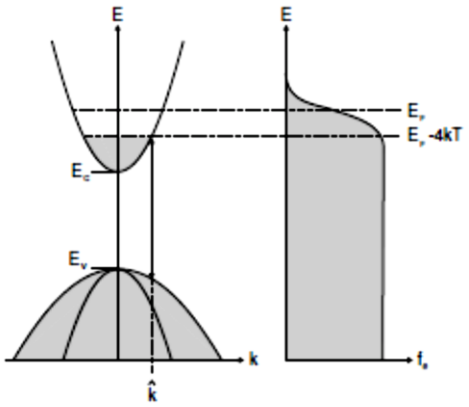

Figure 1.4. Principle of Burstein–Moss shift. Left panel: Schematic band structure with completely filled electron states shown in grey. The k-vector for the lowest photon energy optical absorption process is indicated as ˆk. Right panel: Electron distribution function for a degenerate electron gas with Fermi level in the conduction band.

The "apparent" band gap of a semiconductor can be measured using transmission/reflection spectroscopy. In the case of a degenerate semiconductor, an electron from the top of the valence band can only be excited into conduction band above the Fermi level (which now lies in conduction band) since all the states below the Fermi level are occupied states, this happens about 4kT below E_F [6]. Pauli's exclusion principle forbids excitation into these occupied states. Thus we observe an increase in the apparent band gap, this increase is the Burstein-Moss effect [6].

This reasoning could be quantified and demonstrated starting from the energetic dependence of the band transition

$$E = E_G + \frac{\hbar^2 k^2}{2m_e^*} + \frac{\hbar^2 k^2}{2m_h^*} = E_G + \frac{\hbar^2 k^2}{2m_r^*} \tag{1.6}$$

where m_r is the reduced effective mass of electrons and holes. Considering the energetic conditions described above

$$k = \sqrt{\frac{2m_r}{\hbar^2}(E_G - E - 4kT)} \tag{1.7}$$

So, the Burstein–Moss shift of the absorption edge is

$$\Delta E = \hbar\omega - E_g = (E_F - 4kT - E_c)(1 + \frac{m_e}{m_h}) \tag{1.8}$$

The band gap of TCO is typically studied using the graphic instrument of Tauc plot, that is the absorption profile of the material around a spectral range of the energy corresponding to the inter-band excitation.

The absorption coefficient could be express by this equation

$$\alpha = C\left(h\nu - E_g\right)^{\frac{1}{r}} \tag{1.9}$$

where C depend on temperature and on the reduced mass of charge carriers, exploiting this expression we can obtain that the intercept of an α^r graphic in function of hv, identifies the E_g value, which is the optical gap.

The exponent r depends on the type of transition, for a direct band gap material it is equal to 0.5, while for indirect band gap material is equal to 2. We can see an example of a Tauc plot for a TCO material in figure 1.5.

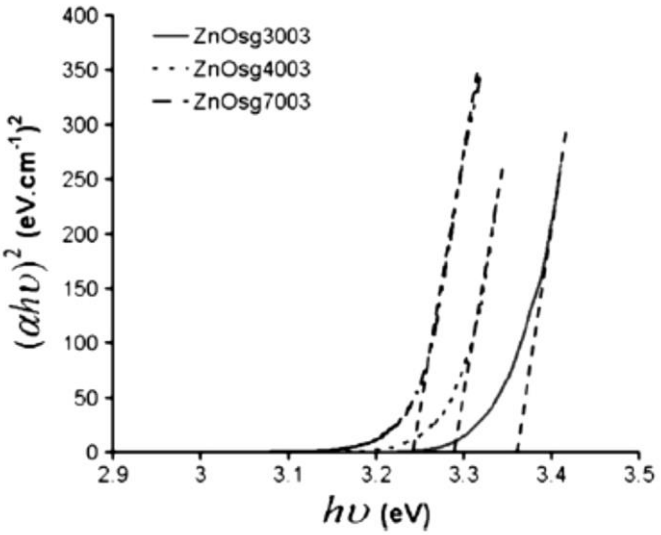

Figure 1.5. Tauc plots of ZnO annealed at 300 °C (solid line), 400 °C (dotted line) and 700 °C[7].

From a more practical point of view, transmission and absorption phenomena are measured and plotted on graphics in function of the wave frequencies, thus is argued in section 2.3 for optical measurement set up description and in section 3.2.4 for experimental results.

1.1.2 Electrical transport properties

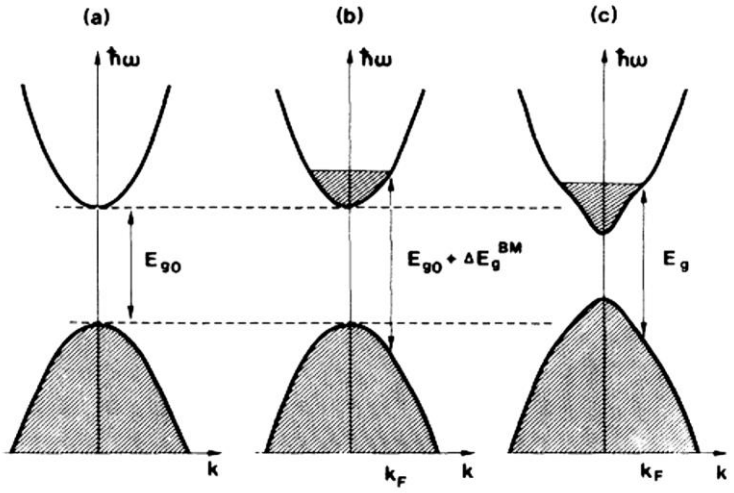

Figure 1.6. Band structure of a general intrinsic semiconductor (a), doped in a degenerate manner with a band gap increase for the Burstein-Moss effect (b) and considering many body effects (c).

For a better comprehension of transport properties I introduce a description of the electronic band structure (figure 1.7) of indium oxide In_2O_3, on which a substitutional doping with tin oxide SnO_2 was made. This material is widely known as Indium Tin Oxide (ITO), probably the most used TCO in opto-electronic applications.

In this case is obtained $In_{2-x}Sn_xO_3$, where x is tin atomic ratio. Tin is tetravalent, therefore, if it occupies a In_{3+} site, it provides one free electron. Moreover the presence of lattice vacant site, as a consequence of doping, release other free electrons: at every oxygen vacancy ($InO_{3/2-x}\square_{1/2+x}$, where □ is a vacant lattice site), missing electrons belonging to 5s In_{3+} orbital, which are not captured by O^{2-} ions, create two electron energy levels for every level near the conduction band (this band is located about 30 meV under conduction band [8]).

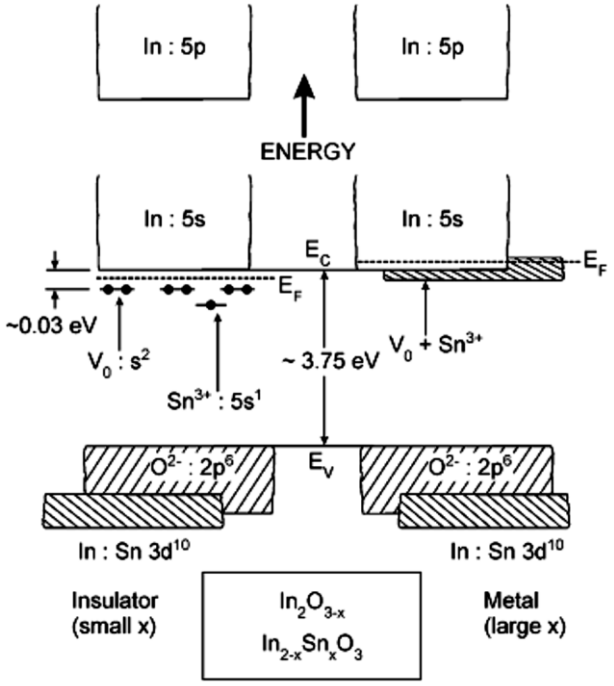

Figure 1.7. Doping effect with Sn on indium oxide bands. X is the Sn rate, V_o oxygen vacancies.

On the left part of the figure 1.7 the 5s band of indium is represented separated from the valence band (energy levels of O_2 $2p^6$ and of In $3d^{10}$ are considered) by the energy gap, are also represented the energy level provided by Sn_{3+} ions and by oxygen vacancies V_O. On the right side it is depicted how the system acquires a metal behaviour due to the elevated rate of doping, energy band is filled by delocalized electrons.

After the consideration about the influence of doping on the material's transport behaviour, it is important to underline also the role of mobility for transport properties.

If we considered a low-field transport, we have a proportionality between the drift velocity and the electrical field [6]

$$\mu = \frac{v_f}{\mathcal{E}} \tag{1.13}$$

Where μ is the mobility, v_f is the drift velocity of an electron, and $\mathcal{E}$ is the electrical field. The sign of μ depends on the sign of the carrier; usually it is represented as a

positive number. In an intrinsic semiconductor the mobility is determined by scattering with phonons. Further scattering is introduced by impurities, defects or alloy disorder.

The conductivity is

$$\sigma = ne\mu \tag{1.14}$$

for each carrier type. In the relaxation time approximation the mobility is

$$\mu = \frac{e\tau}{m^*} \tag{1.15}$$

And the conductivity thus

$$\sigma = \frac{e^2 n\tau}{m^*} \tag{1.16}$$

In presence of both electrons and holes

$$\sigma = ne\mu_p - ne\mu_n \tag{1.17}$$

where μ_n and μ_p are the mobility of electrons and holes, respectively.

In a real semiconductor, at finite temperatures, impurities, phonons and defects (finally also the surface) will contribute to scattering. The relaxation time constant summarizes all scattering mechanisms. If the relaxation times τ_i of various processes are independent, the Matthiesen rule can be used to obtain the mobility ($\mu_i = e\,\tau_i / m^*$)

$$\frac{1}{\mu} = \sum_i \frac{1}{\mu_i} \tag{1.18}$$

The different scattering mechanisms have quite different temperature dependences such that the mobility is a rather complicated function of temperature.

As already said, there are different scattering mechanisms which give us different expression of the mobility [6]:

1. Ionized impurity scattering
2. Deformation potential scattering
3. Piezoelectric potential scattering
4. Polar optical scattering
5. Dislocation scattering
6. Grain boundary scattering

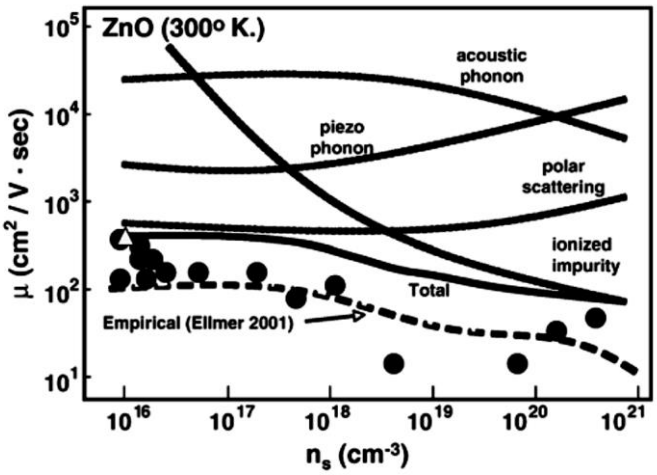

Figure 1.8. Comparison of drift mobility calculations (solid curve) with Hall-effect measurements for undoped and doped epitaxial films (filled circles). The thick dashed line is the experimental fit for ZnO [11].

It is important to point out that the relative weights of these scattering processes depend on the concentration of charge carriers, except for those depends only on structural properties, as defects. In figure 1.8 we can compare different mobility value, for each scattering mechanism, theoretically computed changing n and empirical test. Above a certain carrier concentration it is evident that ionized impurity scattering is the dominant mechanism.

Grain boundary scattering is only significant when grains are smaller than the mean free path of the electron, which is [5]

$$d = \frac{\sigma m^* v_F}{ne^2} \quad (1.19)$$

Phase separation and porosity will result in further scattering. The latter is a particular concern in solution processing, as pores can form when solvent and gaseous decomposition products leave the material. For crystalline TCOs, strict control over the crystalline properties is required. Large grain growth often requires high-temperature processing. However, high temperatures are not compatible with most flexible substrates such as polymers.

In literature [12] theoretical computations, that settle a threshold for the conductivity for a TCO of about 10^5 S cm^{-1}, can be found.

To reassume the topic about resistivity and consequently mobility, I add that many progress has been done to improve these properties, controlling the stoichiometry of dopants or the main feature of the process deposition. Moreover it is not desirable for TCO films to have too high a carrier concentration (>10^{21} cm^{-3}) because of potential free carrier absorption in the near-infrared range, which is a detrimental factor in many applications requiring a wide optical band pass from 400 to 1100 nm [11].

Two approaches can be considered as a means to increase carrier mobility :

- controlling the density of resident defects in order to reduce ionized impurity scattering;
- tailoring the nano/microstructure to reduce the grain boundary scattering.

1.1.3 Durability

Another important property of TCOs to be considered is the durability, which affect the life-time of the entire photovoltaic module. Interaction with environment means the penetration of oxygen or moisture inside the device, with the consequence of electrochemical reaction, structure modifications and finally deterioration. Moisture and organic pollutants penetration could

diminish optical transmittance, this phenomenon is enhanced by structure porosity, this affects also the saturation of oxygen vacancies; for instance Mirjam Theelen at al. [9] found that the migration of H_2O/OH^- produces the formation of hydroxides into grain boundaries, which act as potential barrier to the movement of charge carriers, reducing electrical resistivity and mobility.

Based on these impellent reasons, the PV enhancement has identified the need for improved TCOs, advanced encapsulation, and studies of reliability and long-term degradation mechanisms. For this reason modules are subjected to damp heat test, which consists in the evaluation of the properties of material as they are influenced by the absorption and diffusion of moisture and moisture vapour, in a controlled ambient. Also high temperature processing deteriorate materials, for example considering the fabrication of DSSC, in which temperatures above 400°C are reached [45], the use of ITO is precluded, because it degrades over 300°C.

The importance of the right choice of the material is reflected on the fabricating process of the solar module, moreover an encapsulation procedure and coating could be useful to increase the resistance of the materials to outdoor ambient. The degradation processes affect functional properties depending on the film structure, morphology, thickness and composition. This phenomenon is considered in this thesis work, at section 3.5, about the quick degradation, observed during characterization procedure, of electrical resistivity and transmittance of AZO nanostructured thin films.

1.2 TCOs for photovoltaic applications

TCO are interesting for their capacity in maximising quantum efficiency in a photovoltaic device, in operating as light trapping to enhance optical path through highly diffusive film, in optimizing electron current transport, considering the intrinsic material resistivity and the potential barrier at interfaces of different materials.

The choice of TCO is driven by some considerations, including work function, band alignment, materials compatibility, processing and cost.

An overview of principal materials used for every kind of photovoltaic cell is depicted in table 1.2.

Cell Type	TCO in Current Use	TCO Needs	Materials Goals
Heterojunction with intrinsic thin layer (HIT) cell	Indiun tin oxide (ITO)	Smooth,good interfacial properities,very good conductivity, low temperature deposition, light trapping	Indium zinc oxide (IZO) indium-free materials, ZnO
Copper indium gallium selenide (CIGS)	Intrinsic-ZnO/Al:ZnO	Interfacial stability to CdS, low-temperature deposition,resistance to diffusion and shorting, need to make/improve the junction	Single-layer TCO to replace tro layers and CdS layer
CdTe	(SnO_2) Zn_2SnO_4/Cd_2SnO_4	Stable interface to CdS/CdTe at temperature, diffusion barrier	Doping of ZnSnOx materials, single layer TCO
Nano-hybrid polymer cell	ZnO, SnO_2, TiO_2	Nanostructured with right length scale, work function matching, interface with organic, correct doping level for carrier transport	Self-organized structures core-sgell structurea, new non conventional TCOs
Grätzel cell	TiO_2	Nanostructure with high electron mobility	Improved TiO_2 morphology and possible use of doped materials, new non-TiO_2 materials
Amorphous Si	SnO_2, ITO and ZnO; many cells employ two TCO	Temperature and chemical stability,appropriate texture for both TCO layers	High conductivity, texture and ohmic contact for both TCO layer

Table 1.2. Transparent Conducting Oxides (TCOs) employed in photovoltaic devices [13].

TCOs are used as current-collecting electrode on the sun-facing side of the cell. This is because the lateral conductivity of doped thin film semiconductors that are sufficiently thin to possess high optical transmission is too high for carrier collection over significant distances [45].

They are widespread in thin film solar cells and 3rd generation solar cells as: HIT (heterojunction with intrinsic thin layer), CIGS (copper indiunm gallium diselenide), CdTe (cadmium telluride), OVP (organic photovoltaic) and DSSC (dye sensitized solar cell) cells. That devices are briefly described in this section, underlineing the main features of integrated TCO [13].

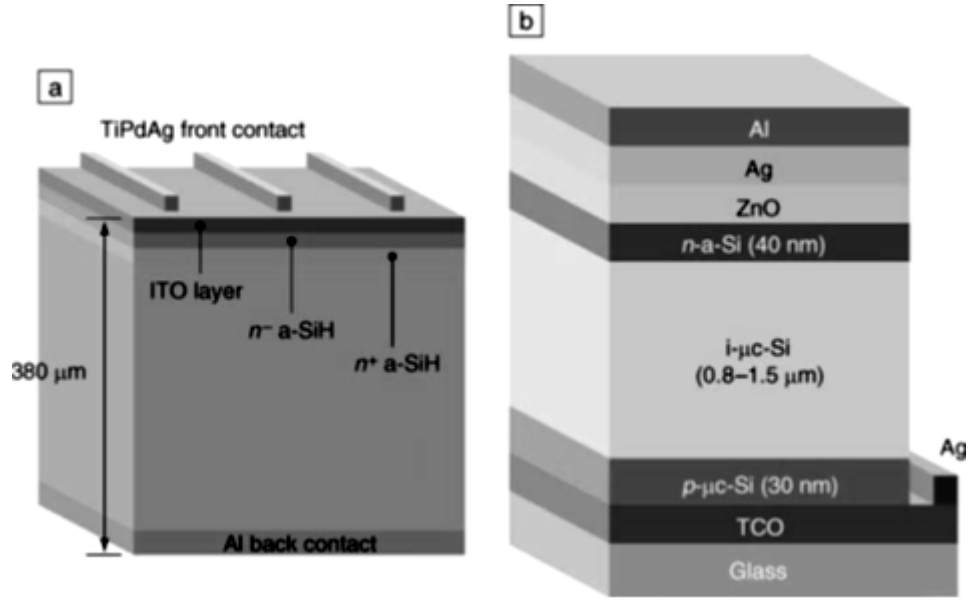

Figure 1.9. Typical configuration for (a) the Sanyo heterojunction with intrinsic thin layer (HIT) cell and (b) an amorphous Si *n–i–p* cell. In (b), i stands for intrinsic, μc is microcrystalline, and a is amorphous [13].

The structure of a HIT cell (figure 1.9a) consists of a crystalline silicon layer with an amorphous top junction in contact with a TCO layer and a metallic collection grid. This technology has achieved efficiencies of up to 19.2% in commercial PV modules. The TCO in this application must be deposited at low temperature, be highly conductive and form a good contact with the *n*+ amorphous Si layer. ITO is the most used TCO in this device, but with the discovery of high-mobility TCOs such as In_2O_3:Ti [46] and

In_2O_3:H [47] it seems likely that the ITO layers in the HIT cell will be replaced by one of these materials before long [45].

Amorphous Si solar cells (figure 1.9b) use TCOs as a top contact layer, as shown in Figure 1b, and in cells fabricated on glass substrates, it is common to employ a second TCO layer on the glass side. The specific needs for the TCOs used in these applications are chemical and structural stability, low cost, and the ability to be easily textured. Surface morphology control is increasingly important to improve light trapping as the Si part of these cells becomes thinner. ITO is generally use but either and either ZnO:Al or ZnO:B [45].

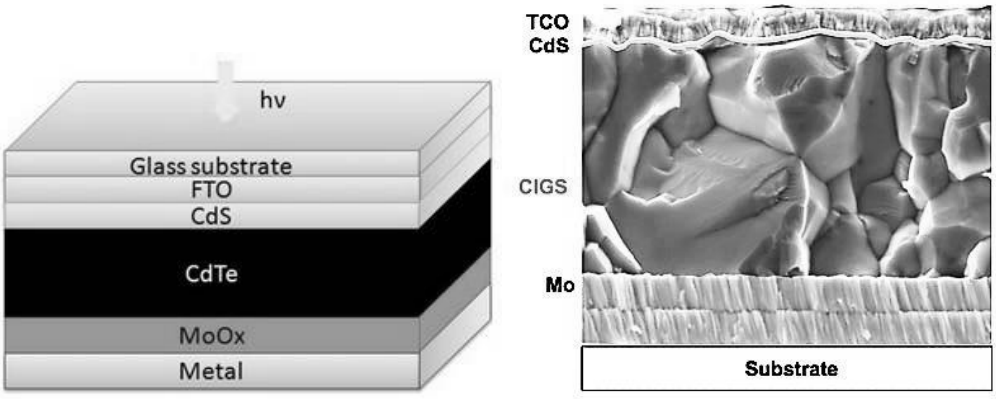

Figure 1.10. On the left side a CdTe solar cell, on the right side a cross section of a CIGS solar cell.

Copper indium gallium selenide (CIGS) and cadmium telluride (CdTe) thin film solar cells have demonstrated efficiencies near 20% in the laboratory and have already begun to transition into commercial production. A CIGS cell is shown in Figure 1.10. The requirements for the top TCO contact in CIGS cells are both demanding and unique to this technology. The defect chemistry of CIGS is complex, and the active layers in these cells are highly temperature-sensitive and susceptible to defect and impurity diffusion. To maintain stoichiometry at the surface and to prevent point defect creation caused by selective evaporative loss at the surface, a stabilizing thin layer of CdS is used to cap the CIGS and to form the initial contact junction with the

TCO layer deposited above it. Typically the TCO used in these applications has been Al:ZnO.

As shown in Figures 1.10, the CdTe-based solar cells have an inverted geometry relative to CIGS, and consequently the demands on the TCO materials during processing are more severe, since they are exposed to a high-temperature CdTe deposition step. This means that the TCO must be resistant to diffusion from both sides during the high-temperature deposition of the CdTe layer while remaining conductive and transparent. Superior optical performance can be obtained with a TCO consisting of Cd_2SnO_4.

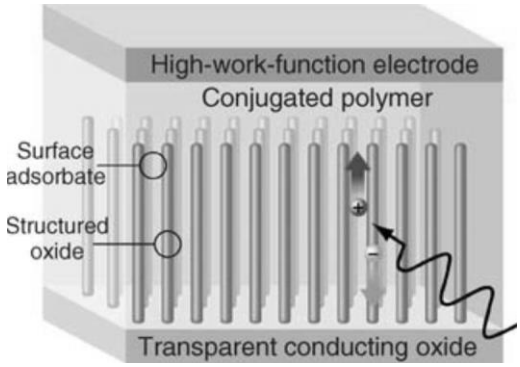

Figure 1.11. Schematic view of an organic photovoltaic cell using a nanostructured transparent conducting oxide (TCO) grown on a planar TCO layer and intercalated with a conjugated polymer [13].

Organic photovoltaic (OPV) devices have recently emerged as a natural extension of the success of organic light-emitting diode (OLED) technology. This approach to PVs is of great interest because it could potentially be implemented as a low-temperature, low-cost, large-area technology. Initial device efficiencies of nearly 5% have been obtained, and the improvements needed for higher efficiency have been identified. The needs of the TCO in an OPV device include work–function matching, stability on a flexible surface, the ability to protect the OPV layer from the atmosphere, and low resistivity. These requirements make the organic transparent conductors unusable for this application. Inorganic TCOs, however, are suitable and also offer the possibility of being nanostructured into filaments to maximize the organic/inorganic interface and

to minimize the impact of the short diffusion lengths on exciton dissociation and charge carrier collection. The ideal TCO for OPVs must also have a high work function to optimize the open-circuit potential and to facilitate charge injection and also be readily wetted by the organic layer. Finally, the ideal TCO would have high mobility and high carrier density when processed using a non-vacuum, low-temperature-based deposition approach. No such TCO currently exists, but a conceptual diagram for a nanostructured TCO/polymer cell is shown in figure 1.11. Attempts to realize this design with a non-optimized structure using ZnO nanorods and an organic (P3HT/PCBM) fullerene blend have achieved nearly 3% PV efficiency. As indicated, there is a tremendous amount of optimization needed for the TCO in this application, and it is likely that existing choices will not be adequate.

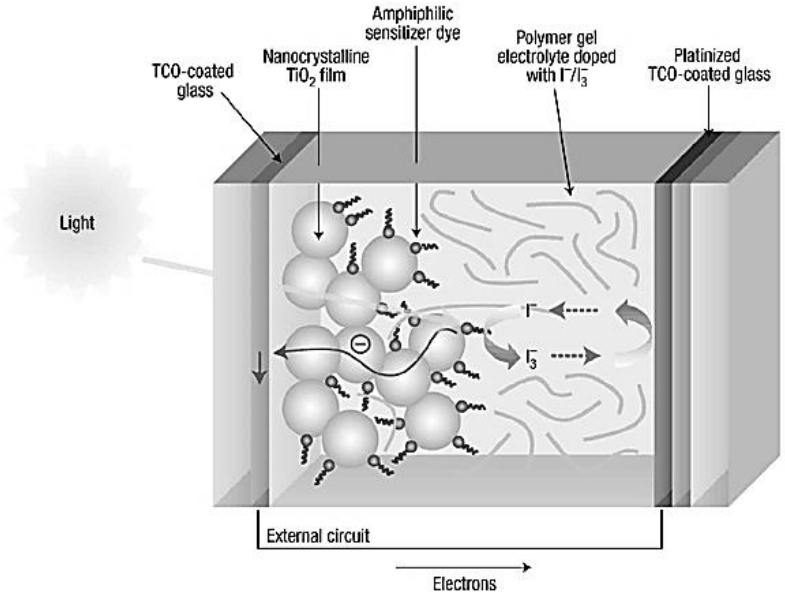

Figure 1.12. Schematic view of the Grätzel cell, showing the use of a TCO from con tact and dye-sensitized nanocrystalline TiO 2 particles.

The Grätzel cell, illustrated in figure 1.12, is an innovative approach to PV that uses nanoparticles of dye-sensitized TiO_2 to collect electrons from electron–hole pairs created by photon interaction at a dye/TiO_2 interface. The holes are transported via aqueous ionic mediators for collection at TCO counter electrodes. This technology depends functionally on the use of optimized TCOs. Typically, low-cost F:SnO_2 or ITO

are used as the back contact for the undoped nanostructured anatase TiO_2. The transfer of holes to the TCO front electrode is aided by a thin, discontinuous coating of Pt particles that speed the electron transfer kinetics. Like the OPV devices described in the previous section, rapid, facile injection of carriers into a TCO with sufficient mobility is critical. This means that the interfacial properties of the oxide, chemical stability, conductivity, and interface to the conventional TCO are all important. Recent work on the doping of anatase to create a conductive TCO may present opportunities for device optimization. In addition, there is an increasing volume of work on TiO_2 and other oxide nanostructures grown by low-temperature solution processes, such as the anodization of Ti metal to form TiO_2 nanotubes. This body of work has opened the synthesis of oxide nanostructures as a large new area of TCO research that may significantly impact Grätzel and OPV devices.

The research of TCOs is investigating aspect commune to every type of solar cell: as the development of new materials, such as bilayer [45] TCOs, which exploit properties of more materials, or amorphous TCOs, which their natural large-scale uniformity and absence of boundaries running throughout the film thickness [45] and especially indium-free compounds, cheaper and more available on the market; it is trying to exploit different nanostructures in order to improve some properties already present in compact films, such as the ability to diffuse light increasing for example the haze factor (the ratio of diffused transmittance and total transmittance); therefore must not be forgotten the improvement of some properties like stability or flexibility of TCOs.

1.3 Deposition techniques

As stated in previous section, the most used method to obtain a TCO is the degenerate doping of a metallic oxide.

The most produced are n-doped TCO, because in p-type there is a difficulty of precessing due to the strong holes' localization. This is caused by doping of material, which contribute to the creation of oxygen vacancies that strongly attract.

Electrical and optical properties of TCOs are affected by the deposition technique, from a structural and morphological point of view.

The principal methods used include deposition technique for erosion of solid target (magneton sputtering, laser ablation) and through the use of chemical precursor (CVD, pyrolisis and solutions).

In this section I just introduce some principal techniques, therefor diferent resistivity values for each deposition techniques are shown on table 1.3.

TCO	Deposition methods	Doping element	ρ range(10^{-4} Ω cm)	Band gap (undoped)(eV)
SnO_2	APCVD,spray pyrolisis	F, Sb, Cl	3-8	3.6
ZnO	Sputtering, PLD, LPCVD, APCVD	AL, Ga, B, In, F	1-8	3.3
In_2O_3	Sputtering, PLD	Sn, Mo, Ti, Nb, Zr	1-3	3.7
CdO	MOCVD	In, Sn	0.5-20	2.4
TiO_2	Sputtering, PLD	Nb, N	9-10^6	3.2
Cd_2SnO_4	Sputtering, sol-gel, spray pyrolisis	Self-doped	1.2.-10	3.1
Zn_2SnO_4	RF sputtering	Self-doped	30-60	
$Zn_2In_2O_5$	DC or RF sputtering	Self-doped	2.9	2.9
a-IZO	DC sputtering	Self-doped	3-5	3.1

Table 1.3. Overview of different TCOs, with a comparison between resistivity and band gap [45].

The process I used for my purpose, Pulsed laser deposition, is described in more detail in section 2.1.2, here I just underline the main features of PLD, which is a PVD technique that permits the ablation of a material from a target by a nanosecond pulsed laser and its subsequent deposition on a substrate, which could be at room temperature or heated.

The control of deposition parameters as the type of atmosphere gas and relative pressure into che chamber, distance between target and substrate and temperature of

the substrate gives to the technique an important versatility in obtaining different combinations of functional properties.

Probably the technique most widely used is Magnetron Sputtering (MS), which belongs to Physical Vapor Deposition (PVD) methods: it consists in Ar^+ ion beam, collimated through a magnetic field on a material target, which is eroded by the beam; the target atoms are finally doposited on the chosen substrate. With MS (direct current or by radiofrequency) it is possible to fabricate films with a wide surface area, thanks to a precise control of growth rate by tuning the deposition parameters as Ar pressure, sputter and substrate voltages, substrate temperature and deposition rate.

The setting of these parameters allows us to have a higher control on film structure and performance: a high temperature of the substrate ensures a smaller resistivity [14] due to the increase of the grain dimension [15] and also pressure influences material properites, its increase causes decrease of resistivity and increase of optical transmittance [10].

Solutions techniques are an other important cathegory of processes, which allow the deposition of films at atmospheric pressure with minimal equipment cost. Scalable deposition methods that permit a uniform, large-area coverage are important for high through-put industrial applications.

Coating techniques can be classified into two categories: direct growth of the material on the substrate during deposition or liquid coating that requires additional processing to remove solvent and yield the desired phase. A general schematic procedure is depicted in figure 1.13.

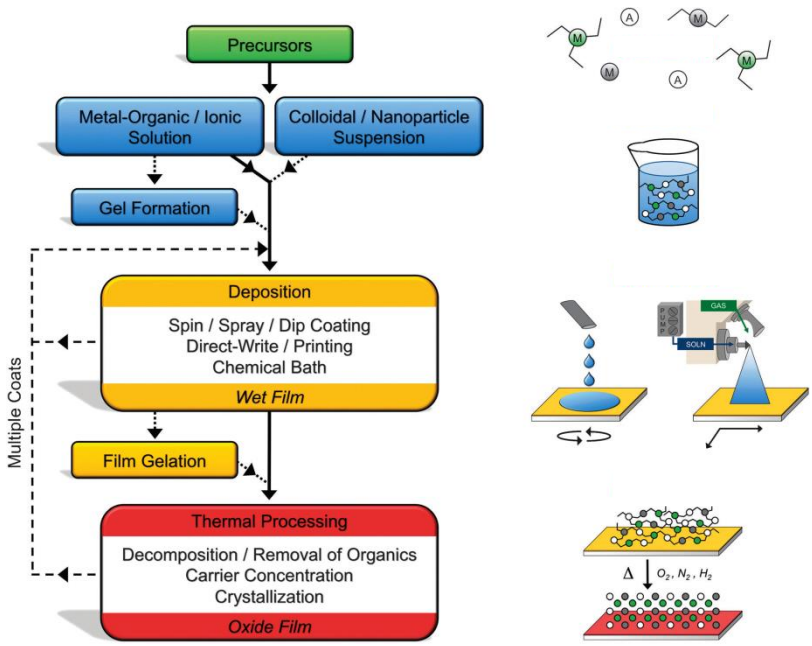

Figure 1.13. Flow chart of typical solution processing routes. Simplest route denoted by continuous line. Alternative pathways denoted by dotted lines [3].

Direct growth methods include electrochemical and electro less chemical bath deposition (CBD). CBD methods rely on the controlled reaction and precipitation of reagents in solution. Nucleation and film growth occurs on the surface of a substrate immersed in the solution bath. The main drawback of CBD is the quantity of solution waste.

Spin-coating is extensively used for smaller, laboratory-scale device processing due to its simplicity and high reproducibility. During the process, the substrate is secured to the spin-coater by a vacuum chuck, and an excess of solution is applied to the surface. Then the substrate is rapidly accelerated (typically to several 1000 RPM), which drives solution flow radially outward. A uniform, thin film is left after spin-off and solvent evaporation. These methods involve application of a coating solution, which is then distributed, smoothed, and thinned across the surface of the substrate with a blade or rod.

Spray-coating is an attractive non-contact, large-area deposition method. It can be used as either a liquid coating method or for the direct growth of films if the substrate

temperature is above the decomposition temperature of the precursors. This later method is commonly referred to as spray pyrolysis. In general, a atomized solution is generated pneumatically or ultrasonically and then directed onto the substrate with a carrier gas. Spraying requires low viscosity solutions (typically ≤10 cP).

Those are just examples of a wider category of processes, a more detailed overview is provided by Pasquarelli at al. [3], in which could be found an analysis about all materials deposited through this way, information that goes beyond the scope of this work.

1.4 Aluminum doped Zinc Oxide (AZO)

After the overview of the state of the art of TCO and their functional properties, we focus our attention on Aluminum Zinc Oxide (Al:ZnO or briefly AZO), the material characterized in this thesis work.

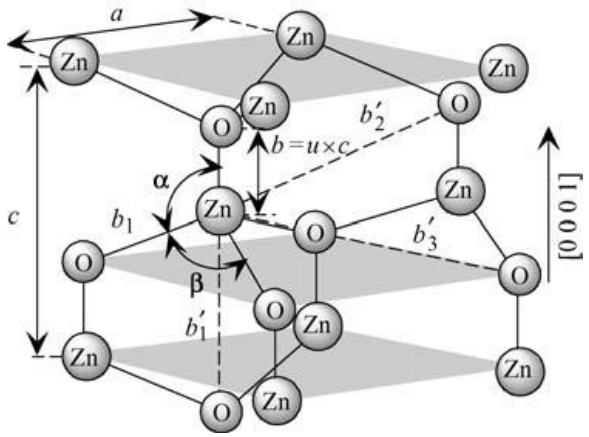

Figure 1.14. Schematic representation of a wurtzitic ZnO structure with lattice constants a in the basal plane and c in the basal direction, u parameter, which is expressed as the bond length or the nearest-neighbour distance b divided by c (0.375 in ideal crystal), a and b (109.47° in ideal crystal) bond angles.

Zinc oxide crystallizes at ambient temperature in the hexagonal wurtzite structure (figure 1.14); doping with aluminium is used to obtain AZO compound and to increase electrical conduction of the pure material, as described in previous chapter: Al^{3+} ions substitute Zn^{2+} ions in the relative lattice sites and allow the formation of oxygen vacancies, which provides more free electrons just beneath the conduction band, about 30-50 meV below. A substantial increase of carrier density between ZnO and AZO, of about four orders of magnitude (10^{17} cm^{-3} against 10^{21} cm^{-3}), is observable [17]. For the AZO used in this thesis work a 2% wt of Al_2O_3/ZnO is used, which coincides to a minimum of resistivity for this material [18,19].

As stated before, an increment in the Al content has important consequences: an increase of carrier density implies a drastic reduction in carrier mobility due to the

increment of scattering probability; a reduction of the transparent window, due to the shift of the plasma frequency at higher energy values, affects optical properties.

The presence of an excessive concentration of impurities produces some defect states into the gap, which compromise transparency at visible frequency; as consequence of that the behaviour of the material would tend to a metallic one.

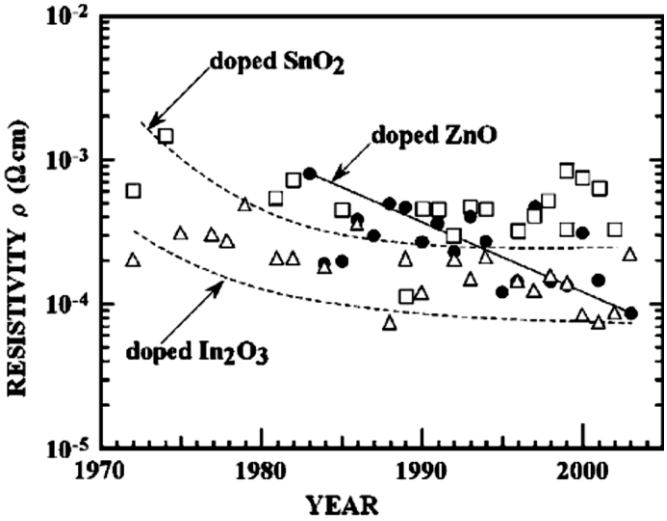

Figure 1.15. Reported resistivity of impurity-doped binary compound TCO films, 1972–present: impurity-doped SnO_2 (□), In_2O_3 (△) and ZnO (●) [1].

Observing the graph in figure 1.15, we can imagine why ZnO was chosen to enhance functional properties for a TCO. The dramatic increase of the demand of indium for numerous application gave rise to a tremendous increment of costs, which obliged to find an alternative to this material. Therefore the presence of In on the earth is quite poor, so the attention turned on zinc, an extremely present material on earth crust, cheaper and with outstanding potential to improve its properties, as shown in the figure 1.15.

The use of AZO is actually widespread in the photovoltaic field, like in CIGS polycrystalline cells as transparent electrode, this induces us to operate to increase light trapping ability, without altering the ability of electrical transport, changing its structure and morphology.

Research is particularly active with the intention to use AZO to replace ITO for transparent electrodes, in particular it regards hybrid cells of type inverted bulk hetero-junction.

The deposition techniques used for AZO are more or less the same for general TCOs described previously. Electrical resistivity of different processes are depicted in table 1.4. Most of techniques related to AZO are carried on with a temperature of the substrate above the ambient temperature, in literature is found deposition in an interval from 25 to 680°C [49], and on samples with a compact structure.

Process	ρ (Ω cm)	Reference
DC Magnetron Sputtering	5.58×10^{-3}	[25]
RF Magnetron Sputtering	1.56×10^{-4}	[26]
Sol-Gel method	2.38×10^{-3}	[27]
PLD	5×10^{-4}	[28]
Atomic Layer Deposition	7×10^{-4}	[29]

Table 1.4. Some examples of electrical resistivity for AZO deposited with different techniques, at room temperature.

In next paragraphs structural and morphological analysis, electrical and optical measurements, the effect of annealing on nanostructured AZO samples are reported, in order to reassume previous work about this particular material carried out by researchers and students in the Micro and Nanostructured Materials lab of the Department of Energy of the Politecnico di Milano. The main interest of these works is to study nanostructured thin films, deposed at room temperature, in order to enhance light trapping ability without neglecting electron transport properties.

1.4.1 Structure and morphology

In this section samples deposited with PLD at room temperature, in presence of an O_2 atmosphere, are described. The pressure inside the chamber is set between 0.01 and 200 Pa. The substrates are glass, in order to carry out electrical and optical

measurment (methods and procedures are described in detailed in chapter 2), and silicon, useful for SEM analysis.

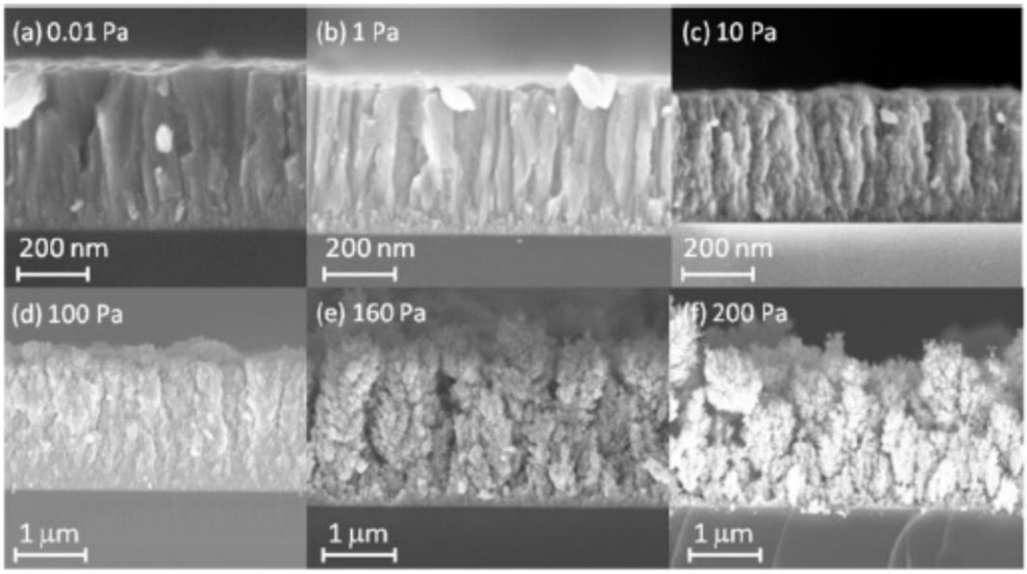

Figure 1.16. Cross-sectional SEM images of AZO films grown at different O_2 pressures [24].

Figure 1.16 shows different AZO morphologies ad different O_2 deposition pressure. A transition from a compact film (with a columnar or pseudo columnar structure) to a porous one, constituted by nanoparticles assembled in a hierarchical, tree-like structure is observed. As the pressurer is increased this important change occurs between 10 and 100 Pa [20], it implies a material density of about 1 gcm^{-3} or less and a higher surface/volume ratio than the columnar structure.

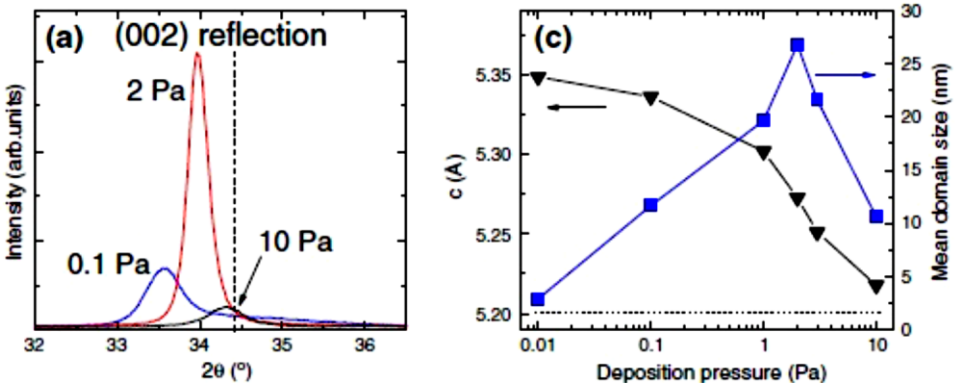

Figure 1.17. (002) peak for AZO films (left) at different deposition pressure and mean domain size and lattice parameter (right) [20].

The structure of compact films has been analysed by X-Ray Diffraction in the θ-2θ direction, this is pointed out by figure 1.17, in which AZO films deposited with PLD present (002) peak of the ZnO wurtzite structure, revealing a preferential (002) growth direction, although for these films the peak is shifted with respect to the reference position of the ZnO (002) reflection (34.44°).

Two different equation are used to obtain the graphic on the right side of the figure above, one is the Bragg's law to estimate the vertical lattice parameter c

$$2dsen\vartheta = m\lambda \tag{1.20}$$

where d is the distance between two adjacent planes, λ is wavelength of incident radiation (in this case 1,54 Å) and θ is the angle that incident radiation forms with crystalline plane. The other one is the Scherrer's formula applied to the (002) peak, from which each domain size was estimated

$$D = \frac{0.9\lambda}{\beta cos\vartheta} \tag{1.21}$$

from this formula a maximum value of domain size of 30 nm at 2 Pa has been evaluated.

From figure 1.17 plots it is evident that the optimal results, considering cristsllinity, are those of the film deposited at 2 Pa. This could be argued by the fact that deposition at low oxygen pressure provides films with a large amount of oxygen vacancies, and it is possible that this affects the correct position of Zn^{2+} ions in the lattice, and with Al^{3+} ions do not occupying substitutional sites. Moreover the large deposition kinetic energy also results in the presence of high stress. As the pressure is increased to 10 Pa, oxygen vacancies are reduced and aluminum ions occupy lattice sites instead of interstitial positions, but the crystalline order decreases probably because of the effect of the background gas which favors cluster nucleation in the plasma plume and reduces kinetic energy of ablated species [21]. So 2 Pa sample could be a good compromise between the number of vacancies and the degree of disorder.

1.4.2 Electrical transport properties

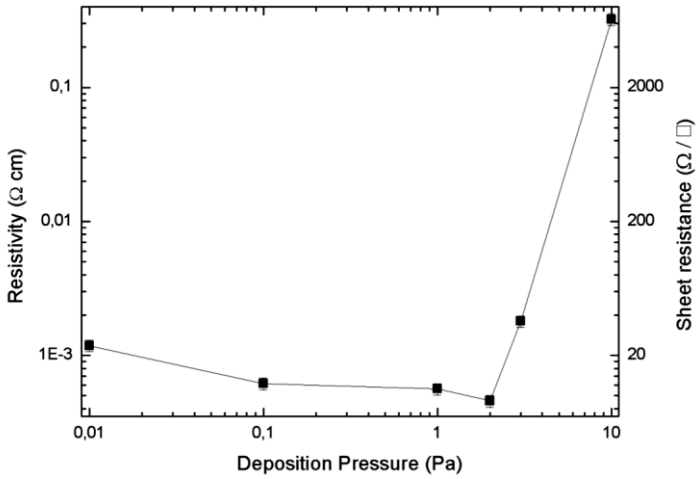

Figure 1.18. Film resistivity and sheet resistance as a function of deposition pressure [24].

In figure 1.18 the trend of resistivity and relative sheet resistance in function of the deposition pressure are shown. Measurements were obtained till 10 Pa, which should be the threshold pressure for the structure transition mentioned in the previous paragraph. So compact films display a conductive behaviour, with a decrement of resistivity until the optimum pressure condition of 2 Pa, with a value of about $4 \cdot 10^{-4}$ Ω

cm [20]. Above 2 Pa resistivity increases drastically and porous films have a insulating behaviour with a resistivity of the order of 1 M Ω.

The high pressure condition results in a higher presence of oxygen in the material, which means the occupation of oxygen vacancy and the consequent reduction of the number of carriers in the valence band.

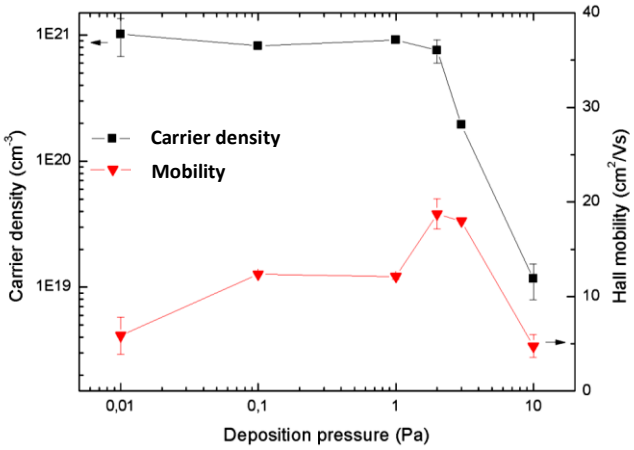

Figure 1.19. Carrier density and hall mobility versus deposition pressure [24].

This is demonstrated by figure 1.19, in which the diminishment of the carrier density with the increase of deposition pressure is visible. Moreover the presence of oxygen at higher pressures negativly affects the mobility of carriers increasing scattering events.

1.4.3 Optical properties

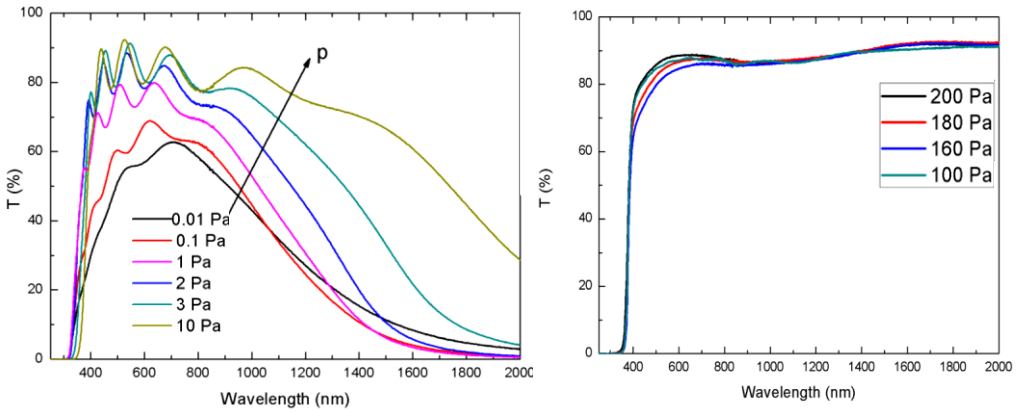

Figure 1.20. Total transmittance spectra of as-deposited films grown at different O_2 pressures, on the left are shown compact films, on the right porous ones [24].

Optical total transmittance spectra for samples grown on glass are shown in figure 1.20. The spectra display an increase in transparency with increasing deposition pressure.

In the region below 300 nm, where photons excite interband electronic transitions, films grown at higher pressures exhibit a sharper absorption profile. The oscillations in the visible range are due to interference phenomena, and their position depends on film thickness and refractive index. The spectra of porous samples do not present interference fringes, due to mesoscale disorder and increased surface roughness. The near-infrared region is characterized by a decrease in optical transmittance due to carrier absorption in the conduction band for samples grown at low O_2 pressures (up to 10 Pa) while porous films show high transmittance up to 2000 nm.

Porous films are characterized by an overall higher transparency, in that the total transmittance is comparable but the thickness is four times as much.

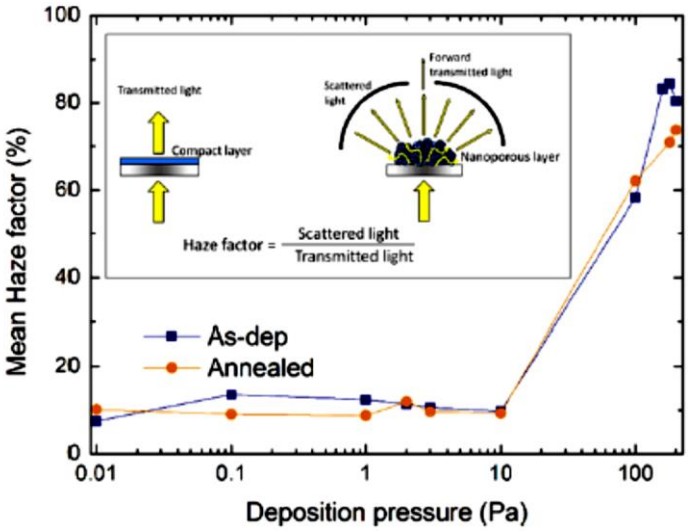

Figure 1.21. The mean haze factor in the visible range (400–700 nm) for as-grown (blue squares) and annealed (orange dots) samples. The inset shows a scheme of the measurement [20].

Light scattering properties were characterized by means of haze factor measurements, i.e. the ratio of diffuse transmittance to total transmittance (see the inset in figure 1.21). Average values in the 400–700 nm range are reported in figure 1.21. The haze factor of compact films is around 10%, for deposition pressures up to 10 Pa. Above 10 Pa it increases, reaching values of 80% and beyond, this is caused by the nanostructure of porous films, which have about the same dimensions of the visible wave lenght; nanostructured porous films show improved light scattering properties, revealing that over 80% of the transmitted photons experience scattering phenomena [20].

1.4.4 Effect of annealing on functional properties

On AZO samples was permormed annealing, which is a post deposition thermal treatment exploited to improve some material properties or to understand specific behaviour occuring in the micro or nanoscale.

In this case samples were annealed in air inside a Lenton muffle fornace at a temperature of 500°C for 2 hour, in order to investigate the role played by oxygen in the film structure and properties [20].

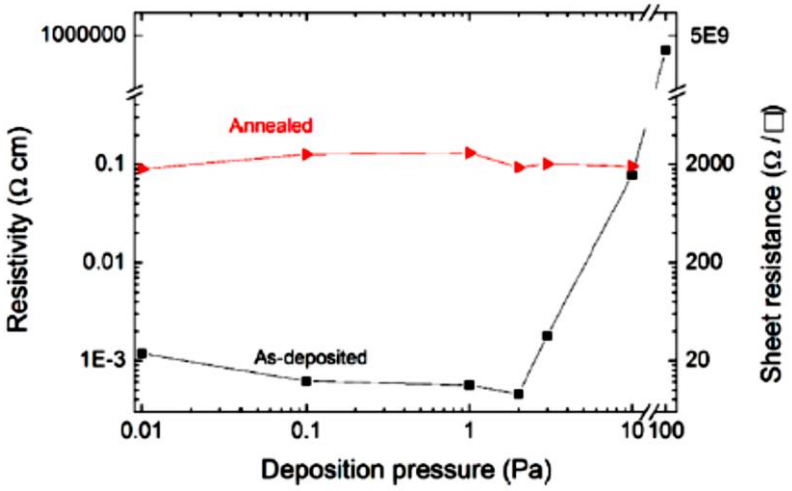

Figure 1.22. Film resistivity and sheet resistance as a function of deposition pressure. The black dots represent as-deposited films, the red triangles are for annealed samples [20].

The resistivity of compact films was measured after the annealing treatment, which induces saturation of oxygen vacancies; an increase in resistivity up to 0.1 Ω cm is observed (figure 1.22), with a trend which becomes almost independent from deposition conditions, reaching the transition pressure.

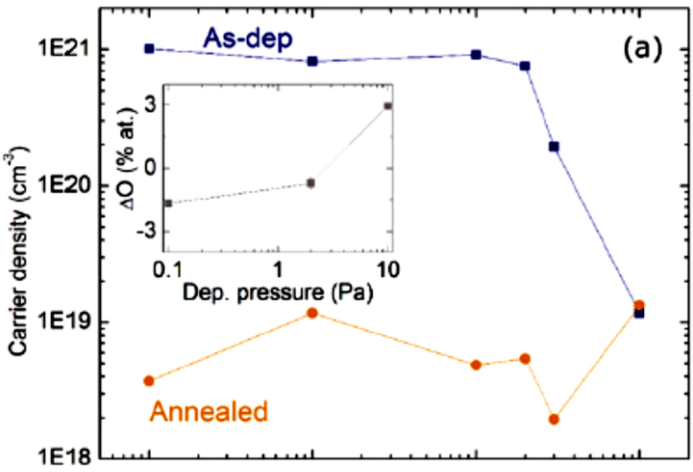

Figure 1.23. The carrier density of compact samples grown at different O2 pressures. The blue squares represent as-deposited samples, the orange dots are for annealed samples. The inset shows the film oxygen content with respect to the AZO target as measured by EDXS [20].

Figure 1.23 confirms this trend also for carrier density, because an increment of oxygen rate has the same effect that we have seen in the previous section about the enhancement of resistivity in films deposited at high pressure. So carrier density is maintained at lower values almost regardless of the pressure.

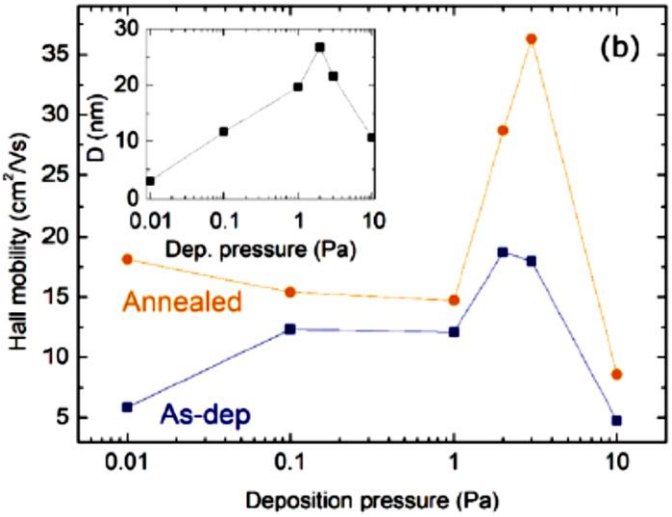

Figure 1.24. The Hall mobility of compact samples. The inset shows the vertical domain size from Scherrer's formula on the (002) XRD peak [20].

Observing figure 1.24 we can say that generally the mobility appears uniformly higher after annealing, this is probably due to a higher crystal order. The trend in as-deposited carrier mobility and that of mean domain size calculated from Scherrer's formula on the (002) XRD peak (bottom inset) are in agreement, suggesting the importance of defects and grain boundary scattering for electrical transport variation.

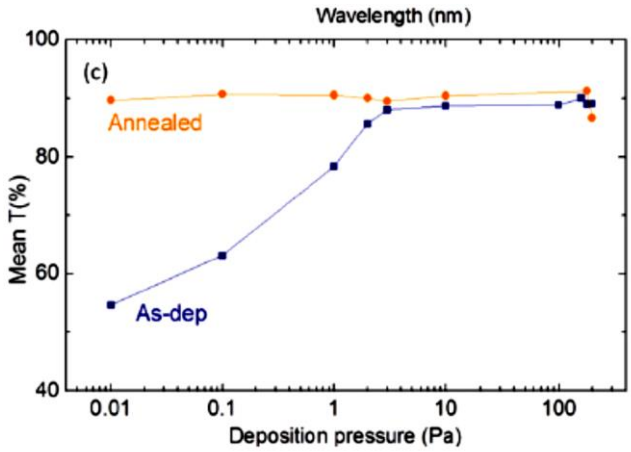

Figure 1.25. Mean transmittance values in the 400–700 nm range for both as-deposited and annealed films, as a function of O_2 deposition pressure [20].

The transmittance values for annealed films (dots in figure 1.25) are sensibly higher than those prior to the treatment for compact samples. The transmittance of porous samples does not vary significantly upon annealing. In general, the variation of transmittance versus deposition pressure for annealed samples is almost negligible [50], it would mean that with thermal treatment oxygen vacancies reach a saturation limit.

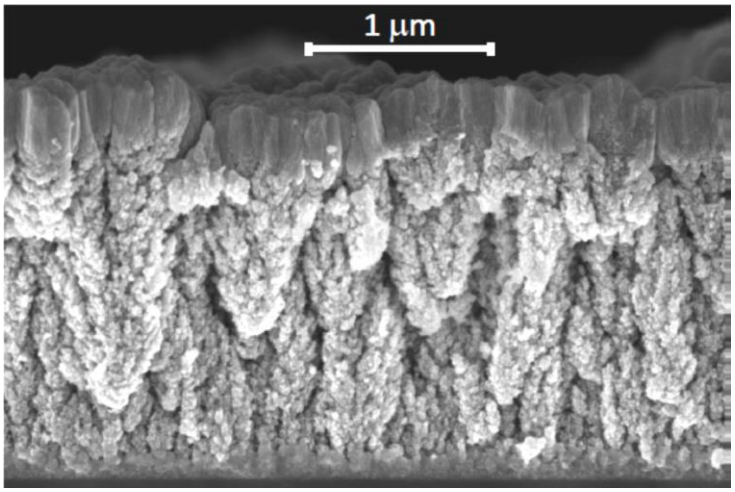

Figure 1.26. Cross-sectional SEM image of a sample grown with a thicker bottom layer grown at 100 Pa [23].

A different approach was considered to improve functional properties of AZO films, this concerns the optimal combination of opto-electronic properties of the compact and porous films. The result consist in a graded film, with a base tree-like nanostructured layer covered with a compact columnar structure [23], depicted in figure 1.26. This could be fabricated changing the chamber pressure during the deposition process.

A first observation of the properties in table 1.5 confirms that a higher oxygen pressure during the growth of the bottom layer increases its porosity and hence haze.

An increase in the deposition time of the bottom layer sorts the same effect, since porosity increases along the direction normal to the substrate, this produce a higher surface roughness, and hence in a less regular coverage by the compact layer. However, a higher effective thickness implies lower total transmittance. The main reason to this difference is found in the significant decrease in mobility due to the lack of a continuous path for charge carriers as a consequence of morphology. Increasing the thickness of the compact layer can significantly increase carrier mobility, but is detrimental for optical transparency [23].

O_2 Pressure (Pa)	100/2
Equivalent Thickness (nm)	1600+250
Mean Total Transmittance	77.07%
Mean Haze	42.39%
Sheet Resistance (Ω/□)	162
Sheet Carrier Density (10^{15} cm^{-2})	15.2
Hall Mobility (cm^2/Vs)	2.52

Table 1.5. Overview of properties of the films shown in figure 3. Mean transmittance and haze have been calculated in the visible (400 nm - 700 nm) range [23].

An optimal combination of deposition conditions was identified by reaching an equivalent thickness of a 100 Pa bottom layer of about 1.6 µm, and 250 nm for the 2 Pa compact layer on the top. The increase in thickness is sufficient to obtain a haze over 40% without compromising total transmittance, which is close to 80%. The transmittance can be controlled by choosing the combination of equivalent thicknesses of the two layers.

It has been demonstrated that a studied combination of the two morphologies can reach an optimized configuration for a TCO used in the photovoltaic field [23].

1.5 Aim of the thesis work

As stated in the introduction my thesis is composed by different procedure and characterization:

- Deposition of samples in a mixed atmosphere of Ar:O_2 at 110 Pa of total pressure and consequent observation of the influence of the change of O_2 partial pressure on functional properties.
- Deposition of one sample in a O_2 atmosphere at a pressure of 2 Pa.
- All the samples before, were monitored to detect a possible variation of electrical transport properties due to the interaction with environment.
- Samples, characterized in previous thesis works, deposed in a O_2 atmosphere at different total pressure, were considered. On these ones electrical and optical measurement were performed in order to estimate possible effect of degradation in a wider range of time.
- Attempts of cross-plane electrical measurements were carried out on porous samples, in order to quantify the anisotropy of the film for these properties.

In particular my research concerns the syntesis of thin films of Al:ZnO with Pulsed Laser Deposition (PLD) at a pressure of 110 Pa in a mixed atmosphere of Ar: O_2, on soda-lime glass and silicon (100) substrate. So, depositing at this pressure level, hierarchical tree-like structure films are considered.

I focused the attention on the influence of the variation of O_2 partial pressure on material functional properties and on the study of the effects of ageing degradation of different AZO thin films .

Different O_2 partial pressure were exploited : 2.5-6-10-15 and 100%. The main reasons for the selected O_2 partial pressure was that, in previous experiment under 2.5% of O_2 partial pressure, samples are strongly absorbing and opaque, for that they are not conform to photovoltaic applications; otherwise, over 15%, the saturation of oxygen

vacancies is too much hight and the film become too much insulating. 100% O_2 is considered just for a comparison.

All of their structures and morphologies were analyzed in cross section with a Scanning Electron Microscope (SEM).

Furthermore electrical measurements were performed in order to obtain in plane resistivity, Hall mobility and carrier density. Also optical measurements were carried out to achieve scattered and direct transmittance.

I also exploited Resistive Thermal Evaporation to deposit four metal electrical contacts on soda-lime glass substrates, in order to better achieve electrical parameters without damaging AZO. Furthermore this process was used to deposit metal contact on AZO in order to perform cross-plane electrical measurements.

The amount of oxygen in the atmosphere of the deposition chamber affects the stoichiometry on the AZO structure. The use of inert gas, like argon, reduce O_2 quantity inside vacuum chamber.

In addition to those samples a compact film at 2 Pa of O_2 atmosphere was deposited. I monitored the variation of electrical resistivity of all these samples to observe the effects of degradation of the material at ambient conditions for a few weeks after deposition, until the resistivity reached a stable value.

I also considered some samples with a compact structure deposited 3 years ago in previous work, to verify ageing over a larger period of time.

Finally some attempts to achieve a cross-plane electrical measurement of porous films were performed, evaporating gold electrical contacts on nanostrtuctured AZO.

Method and techniques used for this analysis are deeply described in the chapter 2.

Chapter 2

Instruments and experimental techniques

In this chapter instrumental set-up and experimental techniques are described. In paragraph 2.1 a brief discussion about the deposition procedures is introduced, in paragraph 2.2 and 2.3 electrical and optical measurements methods are presented.

2.1 Deposition techiniques

2.1.1 Resistive thermal evaporation and electrical contact deposition

In this thesis work resistive thermal evaporation was performed in order to deposit electrical contacts on a substrate.

I exploited this technique to lay a gold thin film, with 50 nm of thickness (nominal measure estimated by a microbalance during the process, maybe real thickness has a little deviation), on a glass substrate. The scheme of the contact configuration is depicted in figure 2.1. The layout is functional to resistivity measurements with a four contact configuration, as described in section 2.2.

Because of the poor adhesion of gold on glass, an interlayer of chromium with a thickness of about 15-17 nm (nominal measure as the previous one) was evaporated.

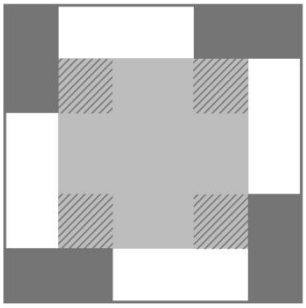

Figure 2.1. Sample scheme: gold electrical contact with a L shape at the sample corner (dark grey) and AZO film in the central square (light grey). All materials were deposited on a glass substrate (white), a square of 1cm^2.

The process consists in the heating of the material until melting point by means of an electrical current passing through a filament or metal plate, used as crucible (shape in figure 2.2), under vacuum conditions. The vapour created by the heating migrates to the substrates. The figure 2.3 illustrates the components inside the vacuum chamber or "bell jar".

Figure 2.2. Crucible used: the shape on the left is used for Cr evaporation, a molibdenum foil was deformed to obtained it; the basket shape is a tungsten filament, used for gold [42].

Samples are positioned above the heat source and fixed on a support at a distance of about 20 cm. A complex vacuum system permits to reach an hypotetical deposition pressure of the order of 10^{-6} mbar.

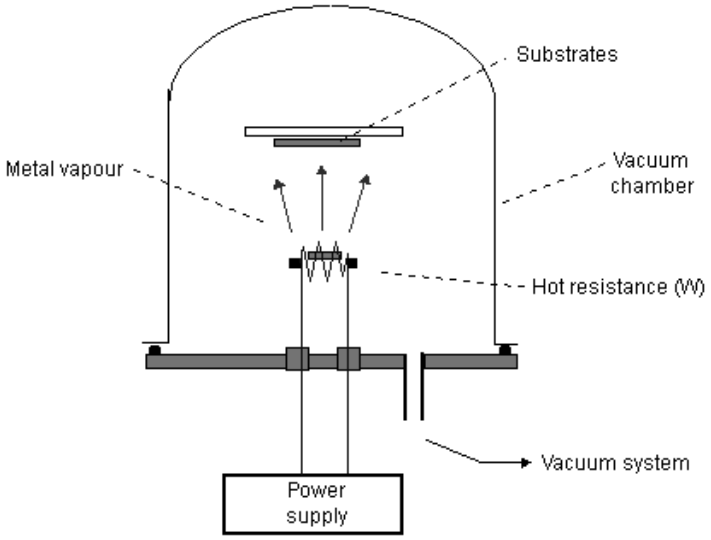

Figure 2.3. Simplified scheme of vacuum chamber.

After reaching the vacuum condition of $6 \cdot 10^{-4}$ mbar with the help of a rotary and diffusive pump [41], an electrical current is injected through the crucible. The amount of current that flows into the circuit depends on the shape and the material of the crucible and on the melting point of the evaporated material. In this case a current of 4 A was exploited to melt Cr and 0.5 A to melt Au, this because Cr has a higher melting point than Au (rispectively 1907°C and 1064°C), therefore a boat shaped Mo plate needs a higher amperage than a W basket filament to heat the evaporant.

2.1.2 Pulsed Laser Deposition of AZO thin film

All the samples analyzed during my research work were deposited with Pulsed Laser Deposition (PLD) on glass and silicon substrates. The process of PLD has demonstrated a great versatility for the production of a wide range of materials such as metals, ceramics, oxides, semiconductors and polymers in the form of thin films and multilayers. In addition it has emerged as a powerful method for the deposition of materials with high complex stoichiometry as in the case of multielemental compounds such as high temperature superconductors, ferroelectrics and for opto-electronic materials.

Laser ablation for thin film growth has many advantages: the energy source is outside the vacuum chamber, which provides a much greater degree of flexibility in geometrical arrangements; film growth rates could be controlled by operating on main deposition parameter.

On the contrary, PLD has some technical and fundamental drawbacks that make this techniques more disadvantage to be used in commercial field: as the production of macroscopic ejecta during the ablation process; impurities in the target material; crystallographic defects in the film caused by bombardment by high kinetic energy ablation particles; inhomogeneous flux and angular energy distributions within the ablation plume, with a consequence of non-uniform thickness. Some of these problems present surmountable engineering challenges (within economic constraints), while others have harder solutions [33].

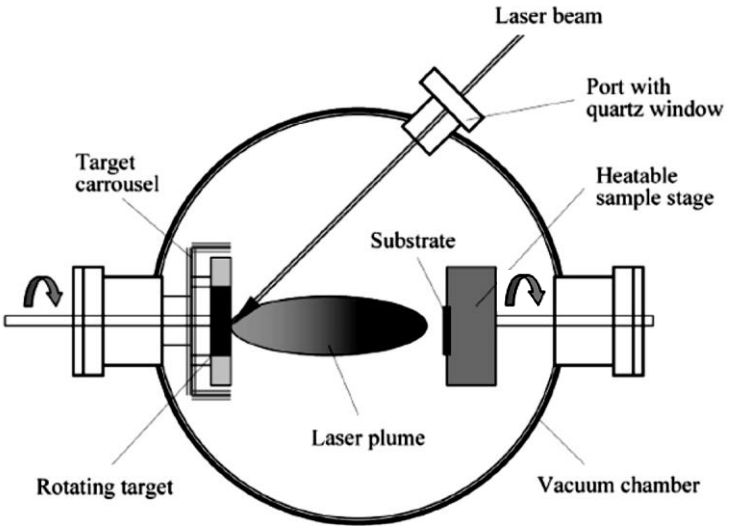

Figure 2.4. Diagram of the apparatus for laser ablation deposition

The operating scheme of the PLD apparatus is depicted in figure 2.4. It is composed by a laser source, a frequency-quadrupled lamp-pumped Q-switched Nd:YAG laser (λ=266nm), which is focalized through an optical system inside a Ultra High Vacuum chamber. It incides with a series of pulses repeated with a frequency of 10 Hz on a target of Al_2O_3:ZnO with 2% wt of alumina. The duration of pulses is 6 ns, with an

energy of 75 mJ which corresponds to a fluence (energy density over a unit of surface) of about 1 J cm^{-2} and a target distance d_{ts} of 50 mm. The rotating system of the target and of the substrate's support are very important: the first one allows a homogeneous wear of the target by the incidence of the laser; the second one permits an homogeneous deposition on more than one target, arranged on the central ring, as depicted by figure 2.5.

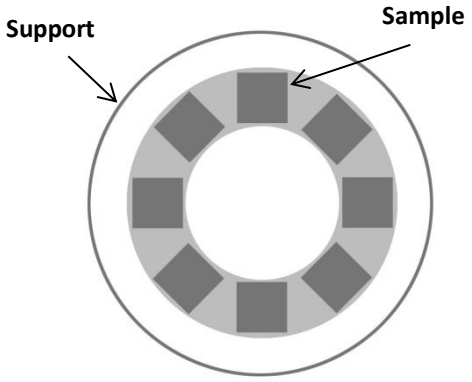

Figure 2.5. Scheme picture of the arrangement of different samples on the rotating support.

The interaction between laser and the material produces the ablation of atoms, which expands as a plasma plume on the substrate.

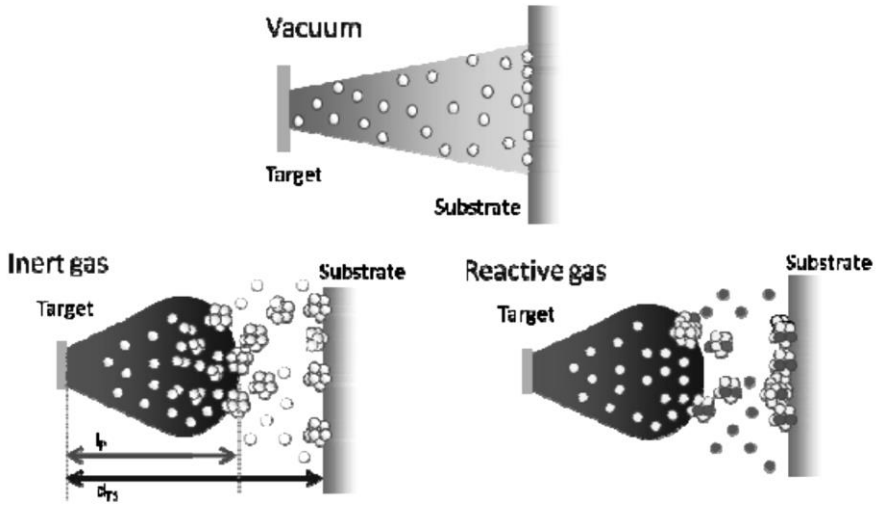

Figure 2.6. Schematic pictures of deposition process for ablation in vacuum, in inert and in reactive atmosphere [30].

Te expansion dynamics in vacuum is characterized by an almost collisionless propagation regime of the ablated species [34]. The spatial distribution is strongly forward directed and the deposition system is mainly characterized by high energetic atoms impinging the substrate. This feature allows atoms to adhere on a substrate and an atom-by-atom deposition of compact films is thus obtained. Contrariwise, when an inert background gas is present in the deposition chamber the light emission increases due to collisions producing radiative de-excitation of the ablated species; the plume edge is better defined due to the presence of a travelling shock wave front. The presence of a background gas produces high pressure, temperature and density gradients at the shock front resulting in strongly out of equilibrium conditions [35], [36].

In the schematic figure 2.6 the spatial confinement favours cluster nucleation in the gas phase during the plume expansion, the diffusion in the background gas favours a kinetic energy reduction. This deposition condition may lead to low energy cluster deposition thus producing a cluster-assembled material in which clusters maintain, at least partially, their structure and properties. If a reactive gas is used as a background atmosphere cluster composition may also be affected by the chemical interaction with the surrounding gas. This permits to deposit aggregates with controlled composition and, for instance, it opens the possibility to deposit metal oxide aggregates by ablating an oxide target in the presence of oxygen; in figure 2.7 the deposition od AZO in $Ar:O_2$ atmosphere is shown [30].

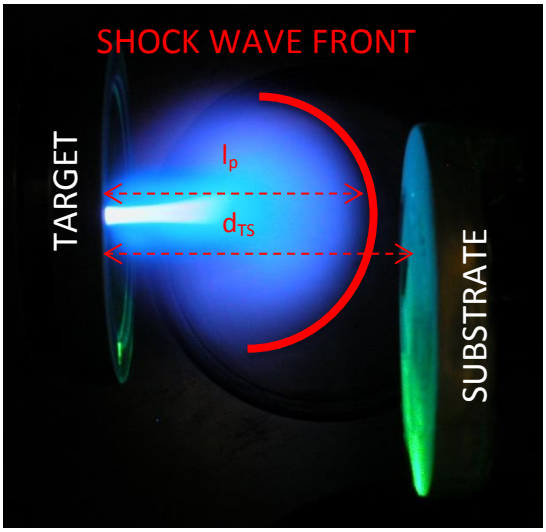

Figure 2.7. Plasma plume producted by ablation of Al:ZnO at 110 Pa of pressure in O_2/Ar atmosphere, with the visible plume length and the target-to substrate distance are indicated.

It is possible to controll the morphology of films at the nano/mesoscale by varying deposition parameters, namely the gas mass and pressure and the target-to-substrate distance with respect to the plume length. In particular we can tune the morphology of the deposited films by varying an important parameter:

$$L = \frac{d_{TS}}{l_p} \tag{2.1}$$

where d_{TS} is the target-to-substrate distance and l_p is the visible plume length [23]. L is a non dimensional characteristic length which indicates the relative position of the substrate with respect to the plume length. In other terms it defines the position of the substrate with respect to the maximum distance of the plume shock front (stopping distance) [37]. Such parameter is defined for ablation in the presence of a background gas for sufficiently high pressures (typically at least abput 10 Pa) to produce a well defined shock front characterized by light emission due to excited ablated species interacting with the surrounding gas [30].

With reference to the L parameter distinct deposition regimes in the presence of a background gas are identified:

- L < 1 (substrate 'in plume'): diffusion of the ablated species in the surrounding gas out of the shock front is strongly reduced. High kinetic energy of the ablated species and reduced cluster growth during the crossing from the target to the substrate are expected;
- L ≈ 1 (substrate 'at the plume edge'): the substrate is placed at about the maximum position of the plume shock front. The expected effect is the increase of interactions between ablated species and the surrounding gas and a reduced kinetic energy of the species;
- L > 1 (substrate 'out of plume'): the diffusion of the formed particles in the gas increases with increasing the L value. As a consequence of the increased scattering with the background gas, the kinetic energy of the species arriving on the substrate decreases.

The L ratio can be used as a control parameter to select the general behaviour of film growth, because the film morphology seems to be related to both l_p and the target-to-substrate distance d_{TS}, of course considering laser parameters (fluence and wavelenght) fixed. L can be used to set a phenomenological relationship and chosen in order to obtain a specific film structure. We can see two different conditions to predict the results of the process: if we have $l_p > d_{TS}$ smooth surfaces and compact films are deposited due to deposition at high kinetic energy. Conversely, if $l_p < d_{TS}$, cluster formation is favoured by plume confinement and also the kinetic energy of the deposited particles is reduced due to diffusion in the background gas before landing onto the substrate (low energy cluster deposition regime), which means the we can obtain the formation of cluster-asssembled nanostructured and nanoporous tree-like structure film. Therefore, the pressure inside the chamber affect the length of the plume and of course the kinetic energy of ablated particles: hight pressure means low kinetic energy, well define plume and low l_p; contrariwise low pressure implies high

kinetic energy and high l_p. The different between a high and low pressure plumes is shown in figure 2.8.

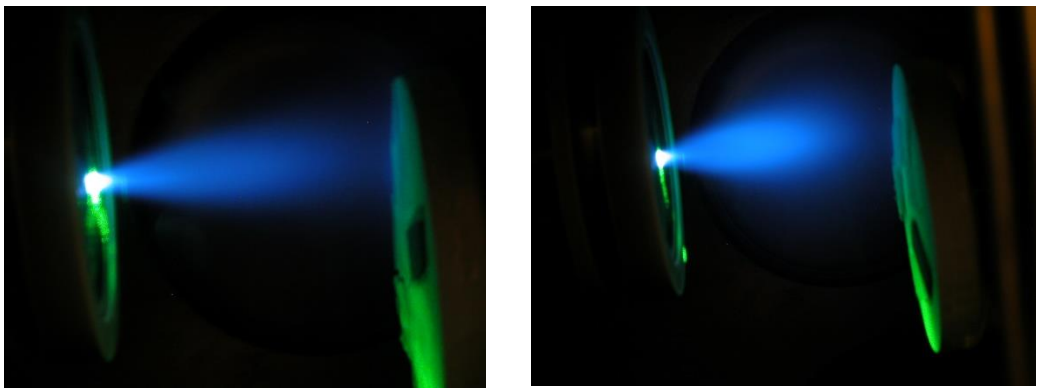

Figure 2.8. On the left picture is shown a plasma plume at about 2 Pa in O_2 atmosphere; on the right one there is a plasma plume at about 100 Pa in O_2 atmosphere.

In this section I provided only few aspects of PLD, in order to better understand how the physics of the process affects the features of the deposited film. A more detailed description does not concern this thesis work, and it is presented by other important references [31],[32],[33].

2.2 Electrical transport properties measurments

2.2.1 Resistivity

Resistivity measurements on samples were performed using the method proposed by Van der Pauw [38].

This technique permits to evaluate resistivity of thin films using two electrical contact as described in figure 2.9: a known current I_{12} flows between two electrical contact 1-2, this implies the presence of a potential drop, which is measured by four other contact on the sample (3-4).

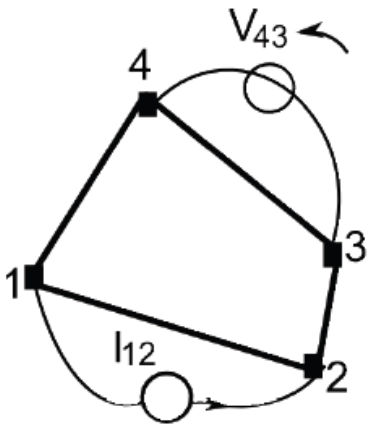

Figura 2.9. Van der Pauw scheme [24].

The Van der Pauw resistivity is defined by

$$R_{12,34} = \frac{V_{34}}{I_{12}} \tag{2.2}$$

the resistivity $R_{23,41}$ is represented in the same way.

Now we define R_S the sheet resistance of the sample, that is the specific resistance over thickness unity (Ω/□)

For this measuerment the following conditions must be manteined:

1. The sample must have a flat shape of uniform thickness
2. The sample must not have any isolated region
3. The sample must be homogeneous and isotropic
4. All four contacts must be located at the edges of the sample
5. The area of contact of any individual contact should be at least an order of magnitude smaller than the area of the entire sample.

therefore, indipendently by the sample's shape, the following Van der Pauw equation is valid:

$$e^{-\pi\frac{R_{12,43}}{R_S}} + e^{-\pi\frac{R_{23,41}}{R_S}} = 1 \tag{2.3}$$

and by definition the resistivity is calculated

$$\rho = R_S d \tag{2.4}$$

where d is the thickness of the film. Configurations with same current in two different directions are considered different. Clearly, for reciprocity theorem is

$$R_{21,34} = R_{12,43}$$

$$R_{32,41} = R_{23,14}$$

$$R_{43,12} = R_{34,21}$$

$$R_{14,23} = R_{41,32} \tag{2.5}$$

and for simmetry

$$R_{21,34} + R_{12,43} = R_{43,12} + R_{34,21}$$

$$R_{32,41} + R_{23,14} = R_{14,23} + R_{41,32} \tag{2.6}$$

All measurements of the more conductive sample have been done with a four wire configuration as shown in figure 2.10. The progressive decrease of electrical properties for porous films forced to change the configuration to a two wire layout: a known current is injected between two contacts and a resistance is measured. The resistivity is obtained by definition

$$\rho = R\frac{A}{l} \tag{2.7}$$

where A is the cross section of the current path and *l* is the distance between the contacts.

Current intensity was supplied by a Keithley 172 multimeter with 3 μA resolution and a Agilent 34970A sistem has been used for voltage measurements with a 10 nV resolution. For change among different configurations an analogical commutator was used. All voltage measurements have been acquired for 10 seconds and averaged to

reduce noise error. Van der Pauw equation is then solved numerically with the Newton-Raphson algoritm [39] by the software MATLAB. Thickness d is measured by a Scanning Electron Microscope and resistivity is then calculated by equation (26). Typical current values used for electrical measurements go from 1 μA for low conductive films to 10 mA for more compact films.

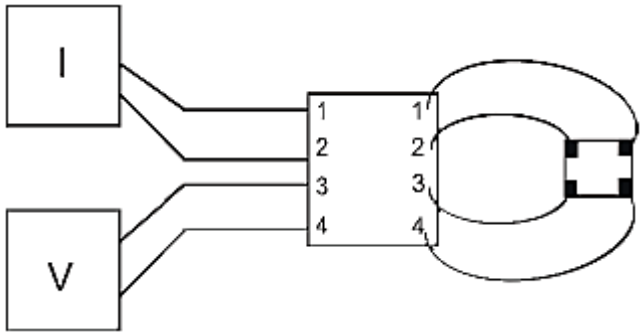

Figure 2.10. Operating sche of the commutator with the four wire configuration.

In the case of two wire configuration the instrument behaves simply as a voltmeter.

2.2.2 Charge carrier density and Hall mobility

The experimental apparatus described in the section before is exploited for the density of charge carrier and hall mobility measurement. As stated in the introductory chapter about TCOs, the behaviour of charge carriers could be described by the Drude model, a classical physical description of the Hall effect [2](figure 2.11).

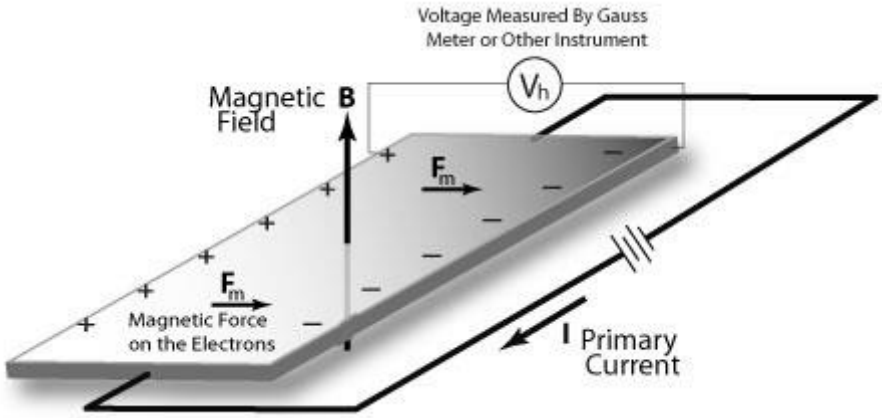

Figure 2.11. Scheme of the hall effect.

In a material crossed by a current I, on which a magnetic induction field B ortogonal to the current flow direction is applied, an electrical potential difference V_H is established, due to the action of the Lorentz force F_m on charge carriers. It can be demonstrated that, defining τ as electron relaxation time after a fast transitory depending on τ , at regime:

$$V_H = \frac{IB}{qnd} \tag{2.8}$$

where *q* is the foundamental electron charge, *n* is the carrier density and *d* is the film thickness. Considering a known injected electrical current and a known applied magnetic field, we can invert the equation (2.8) as follows

$$n = \frac{IB}{V_H qd} \tag{2.9}$$

For Hall effect measurements a four contact scheme is expected. A cross configuration, as shown in figure 2.12, is required. An electrical current is injected through one of the sample diagonals and the Hall potential il measured along the opposite one. The measurement is repeated changing the contacts and current flow direction, as described for the Van der Pauw method.

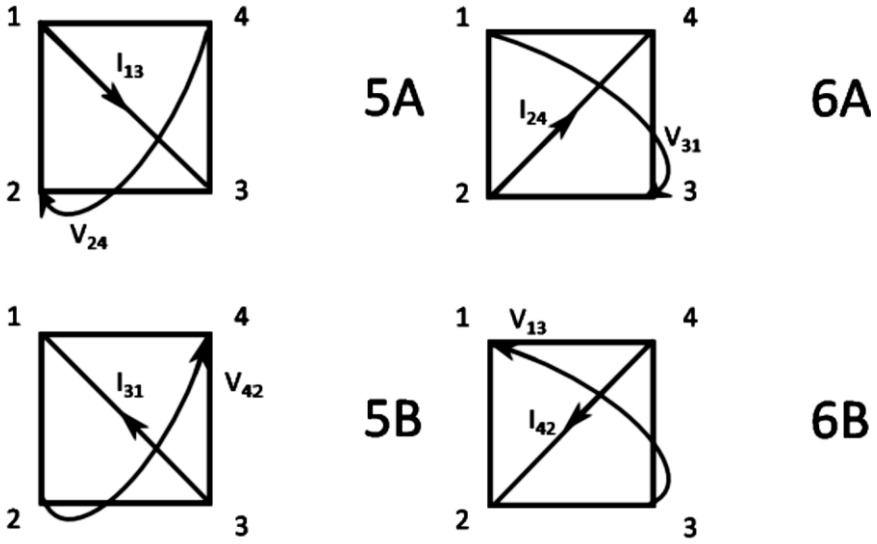

Figura 2.12. Configuration for Hall effect measurement.

For this purpose, the recommended procedure [40] suggests to perform twice all measurements, once with the magnetic field oriented to positive orientation (P) and once to negative (N). Finally, averaging on different data acquisitions, noise can be reduced and we can obtain a value of n from equation (2.9) and μ by its definition

$$\mu = \frac{1}{qn\rho} \tag{2.10}$$

The magnetic field used for this purpose is generated by an electromagnet Leybold 56213, constituted by a solenoid (250 coils powered by a 5 A current). The intensity of the field was measured by a Hall probe. The intensity of the magnetic field is equal to 0.57 T.

2.3 Optical measurements

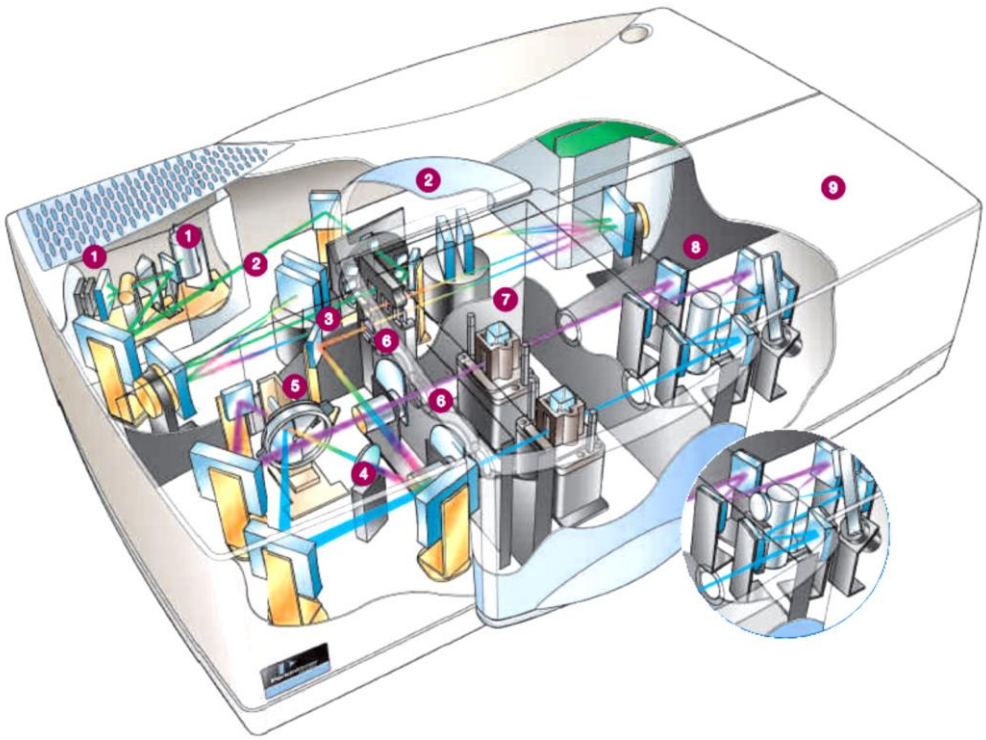

Figure 2.13. Scheme of the spectrophotometer components structure: light source (1), gratinf monochromator (2), common beam mask (3), depolarizer for the common beam (4), chopper (5), attenuator (6), smaple holder (7), photomultiplier and photodetector cooled Peltier cell (8), support for integrating sphere (9).

Optical measurements were performed with a UV-vis-NIR PerkinElmer 1050 spectrophotometer, with component structure similar to the one in figure 2.13. The light source of the spectrophotometer is an alogen deuterium-tungsten lamp and there are two monochromators. They are a holographic grid with 1440 line/mm for ultraviolet and visible and 360 line/mm for infrared. The system has two different detectors, one for high energy and the other for the infrared spectral region. Moreover, an integrating sphere has been used due to high diffusivity of samples deposited at high oxygen pressure. Its role is to collect the transmitted radiation that has been scattered on all solid angle and not only the fraction that has not been

deflected. This sphere has two apertures in front of each other. In one, masked with a metallic lamina with a 3 mm diameter circular hole so as in this range the thickness of the film is almost constant, the light enters into the sphere. The second aperture has a removable shutter. When removed, the no deflected radiation can exit from the sphere without being detected by photorevelator. So, it is possible to separate the direct trasmitted fraction of light from the scattered one through two different acquisition, one for scattered transmittance and one for overall transmittance. As seen before, the ratio between these two quantities is the haze factor. This concept is shown in figure 2.14.

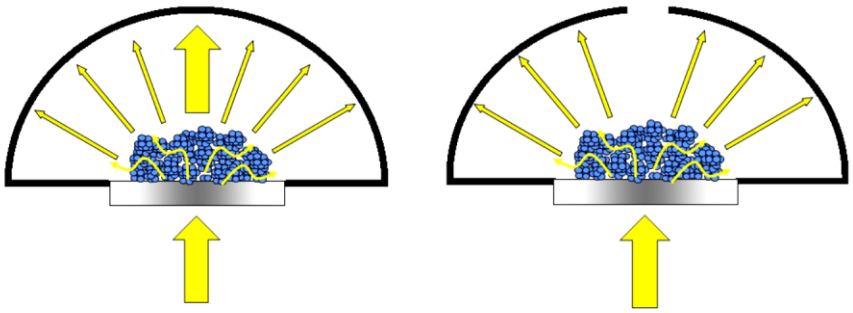

Figure 2.14. Experimental configuration for integrating sphere: on the left scheme for overall transmittance, on the right scheme for scattered transmittance

All spectra were measured with light beam incident on glass substrate first so that it's easy to correct air/glass and substrate interface effects with reference spectrum of bare glass, subtracting it from the total spectrum.

Chapter 3

Experimental results

In this chapter the results of the characterization are presented and discussed. A presentation of all the samples is provided in section 3.1. In section 3.2 the influence of O_2 partial pressure on nanoporous thin films functional properties is described: sampes were measured with SEM and an analysis of different observed morphologies is provided together with thickness measurments; resistivity and Hall effect measurements are shown in order to better understand the role of oxygen content in electrical conduction phenomena. In section 3.2.3 the importance of cross-plane analysis is described, with various attempts to achieve electrical measurements along vertical direction. Finally direct and scattered transmittance are shown with a correlation to light trapping ability.

The ambient and its elements considerably affect functional properties after deposition process; a quick and progressive deterioration of the functional properties of porous nanostructured samples is described in the paragraph 3.3. Moreover older samples deposited at a pressure equal or less than 10 Pa in O_2 atmosphere, so with a columnar compact structure, were analized to estimate a possible degradation of electrical properties.

3.1 Samples description

AZO thin films were deposited on substrates of soda-lime glass, for functional properties measurements and on Si(100), for SEM analysis, by PLD at room temperature. A solid (2%wt.) Al_2O_3:ZnO target was ablated by a pulsed UV laser, described in section 2.1.2 (set up values were maintained constant), the target-to-substrate distance d_{ts} was fixed at 50 mm, with an energy density of about 1 J cm^{-2}. For

nanostructured samples, the background atmosphere was obtained by different combinations of Ar and O_2, reported in table 3.1, flowing in the deposition chamber through a mks 2179a mass flow controller, with a total pressure within the chamber of 110 Pa.

For columnar compact samples the deposition atmosphere was pure oxygen and the total pressure varied between 0.01 and 10 Pa as reported in table 3.2. In all the cases deposition times were selected in order to obtained a desired thickness and previouse experience influenced this choice. Compact samples were deposited in previous work, except for 2 Pa sample 0.8 µm thick, which was growth in this thesis work.

From now nanoporous samples will be mentioned just by the percentage of O_2 partial pressure ($\%O_2$) and compact sample with the value of pressure. Before deposition some techinical issues were present into the laser system, this could affect film growth.

O_2 partial pressure (%)	Thickness (µm)	Deposition time (min)
2.5	1.8	120
6	2.25	120
10	2.4	120
15	3.4	110
100	3	120

Table 3.1. Nanoporous films samples features.

O_2 Total pressure	Thickness (µm)	Deposition time (min)
0.01	0.5	36
1	0.5	36
2	0.5	36
2*	0.8	36
10	0.5	36

* This sample was deposited in this thesis work, otherwise other samples were grown in previous work.

Table 3.2. Compact films samples features.

3.2 Influence of O_2 partial pressure on nanoporous samples

3.2.1 Morphological and structural analysis

A deep analysis was performed with a Scanning Electron Microscope (SEM) in order to understand how a different O_2 partial pressure can affect morphology and structure of AZO films. All the samples considered in this analysis were deposited on a silicon substrate and then cross-sectioned. The thickness of the films were measured and they are reported in table 3.1 with related O_2 partial pressure.

The high deposition pressure produces an increase of collision probability between species inside the ablation plume. Accordingly, we have nucleation of aggregates: these clusters impinge on the substrate with a low kinetic energy producing an assembly of aggregates, which implies a higher porosity inside the film. This can be noticed observing cross-sections of figure 3.1. The importance of O_2 pressure is underlined by the different aggregation into the film, moreover the anisotropic vertical growth is almost lost in lower O_2 partial pressure films. In this kind morphology there is a random orientation of the nanocrystalline structure [20].

Furthermore, looking at SEM images in figure 3.1 the total porosity of the film seems to be different for each films.

A more compact layer is visible at the bottom of the structure, this is typical of the type of growth evolved in this process, after that a more dendritic growth, depending on O_2 partial pressure, is observed.

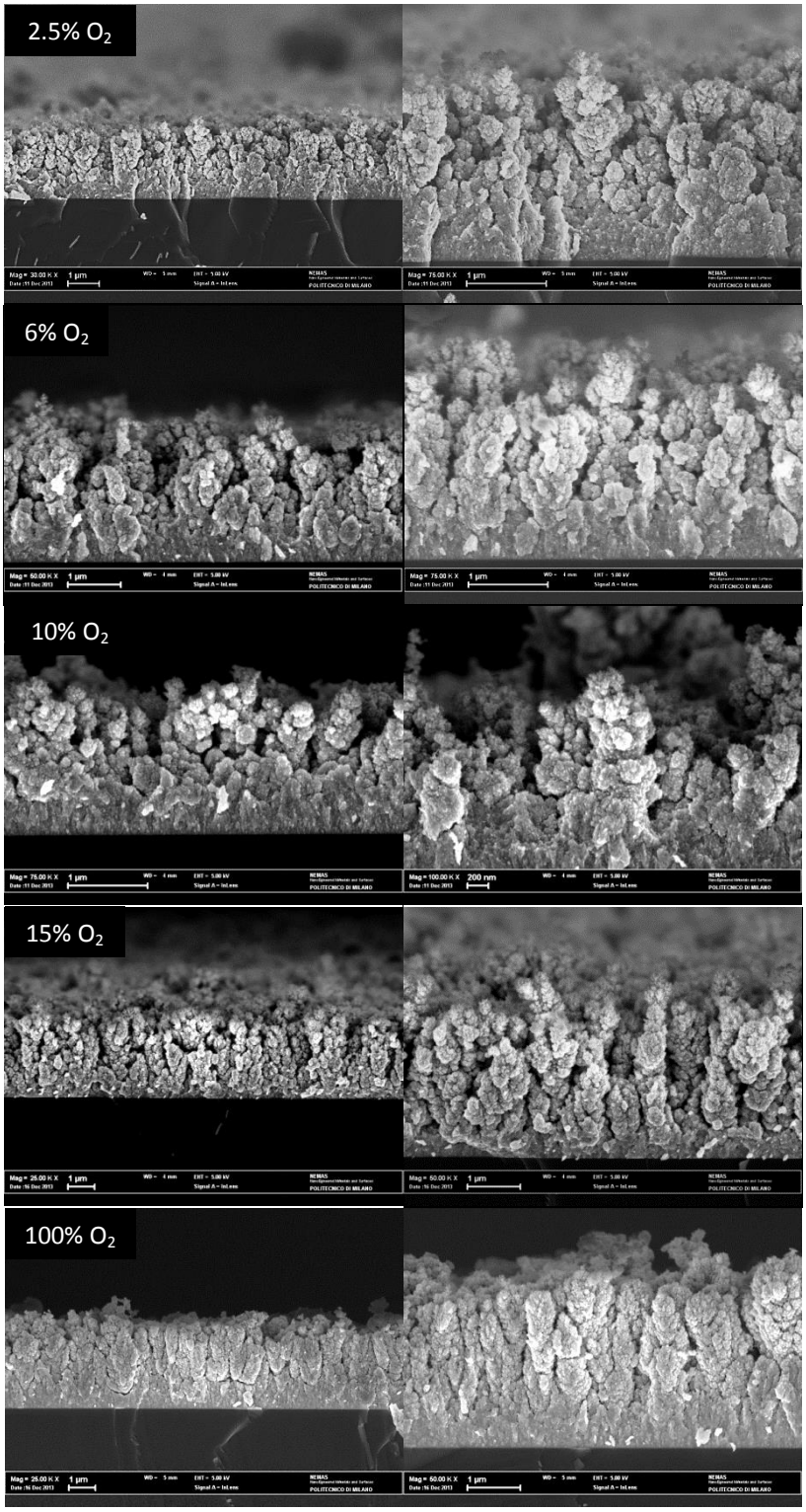

Figure 3.1. Cross-section SEM images of AZO thin film with different O_2 partial pressure

A variation of thickness is reported in table 3.1, the nature of this aspect can be seen in a different aggregation of atoms changing the O_2 partial pressure. Moreover a higher concentration of mesopores can be observed in figure 3.2 into higher O_2 content films, in 100% O_2 the morphology is more like a poplar tree which have a more uniform growth along the vertical direction. In the other films there are bigger aggregates arranged one upon the other along the ortogonal direction with respect to the substrate plane.

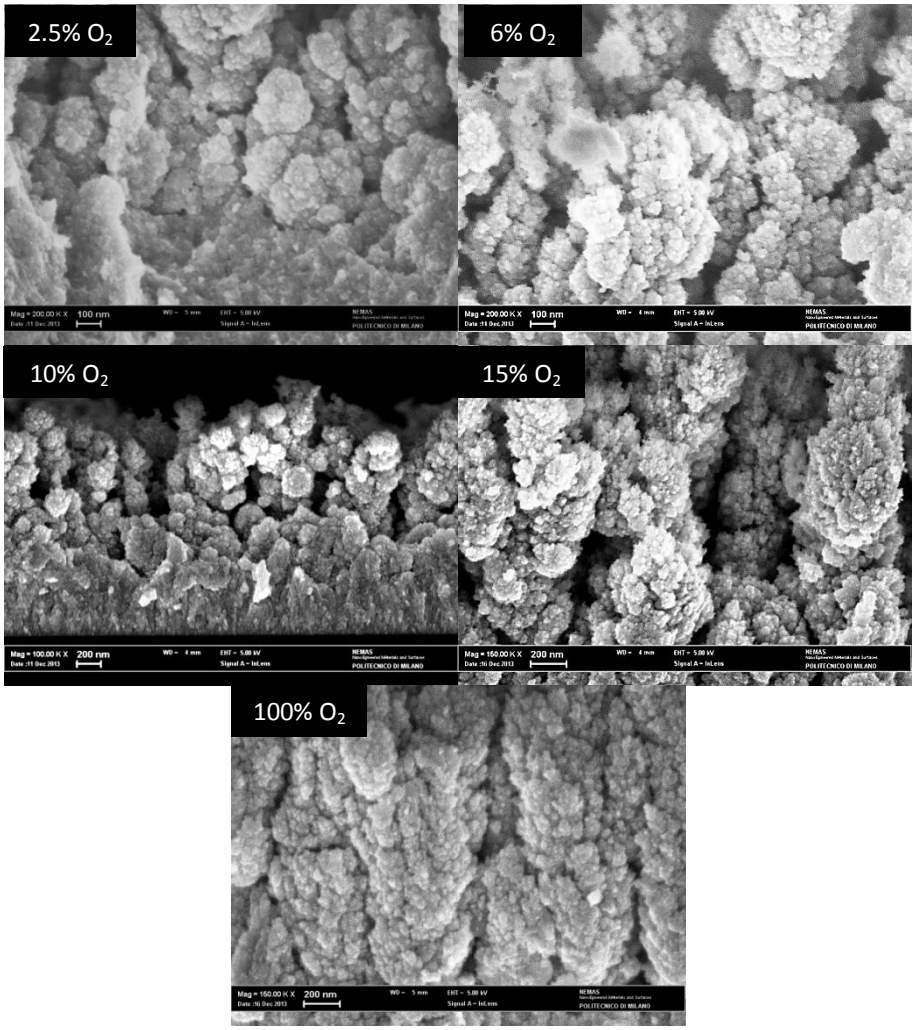

Figure 3.2. Cross-section SEM images with higher magnification of AZO thin film, O_2 partial pressure increases from left to the right and from top to the bottom.

3.2.2 Electrical transport properies

In this paragraph a correlation between O_2 partial pressure and electrical transport properties is performed. In particular cases electrical resistivity, carrier density and Hall mobility were obtained, by means of the methods described in section 2.2.

In-plane electrical properties were measured in the 2-point (for resistivities of 100 Ω cm and higher) in the 4-point probe (for resistivities up to 100 Ω cm) configurations with a Keithley K2400 Source/Measure Unit as a current generator (from 100 nA to 10 mA), an Agilent 34970A voltage meter and a 0.57 T Ecopia permanent magnet.

Using electrical contact configuration depicted in figure 2.1, the measurement is performed at the bottom of the film and a possible current path is shown in figure 3.3.

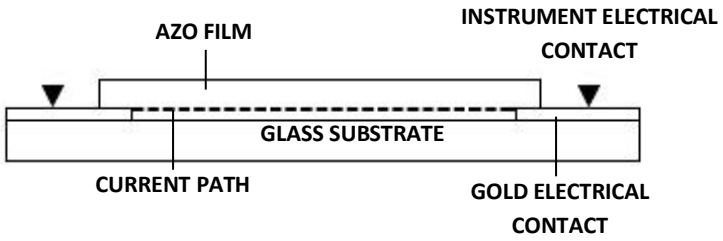

Figure 3.3. Current path between two electrical contact.

This contact configuration allows to avoid a film damaging due to the pressure of pointed electrical contact, that effect is described in section 3.3. Some measurements are also performed on the top of the film, but the different resistivity value can be related to the damaging of the film surface (proved in section 3.2.3) and maybe by the thinning caused by the crush of pointed electrical contacts.

The trend of resistivity versus O_2 partial pressure is shown in figure 3.4. It can be seen that an increment of O_2 partial pressure corresponds to an increment in resistiviy of porous films. In the range of 6 and 10 % we have a not significant variation of resistivity; this could be in contrast with the general trend of resistivity depending on oxygen partial pressure, which are correlated, the value in the graph could be affected by noise measurement or possible gold electrical contact deterioration. Precisely the minimum corresponds to a value of $3{,}17 \cdot 10^{-1}$ Ω cm for the 2.5% O_2 sample, which is far

away from the optimal value measured for compact sample, but we have an important decrease compared to the value of the samples deposited with 100% O_2 content, which was of the order o 10^5-10^6 Ω cm [24].

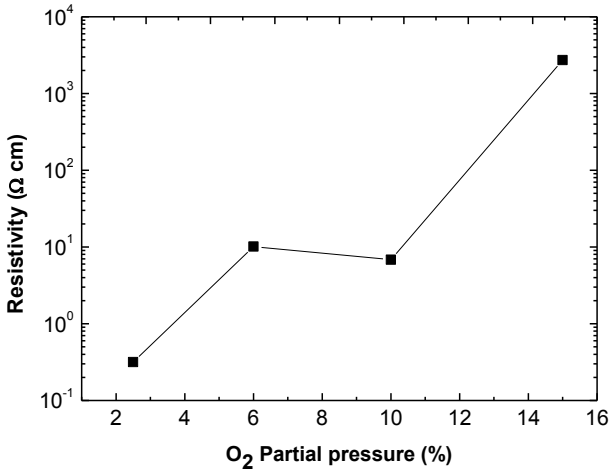

Figure 3.4. Resistivity versus O_2 partial pressure.

This value was not measured with the same configuration and instrument of this thesis work, since the four wire configuration was not possible to measure resistivities of samples with a O_2 partial pressure equal or above 15%, because they are too high and instrument measurement ability is out of that range. As stated before, the value of resistivity of the 15% reported in figure 3.4 was obtained with a 2 wire configuration. Increasing the oxygen partial pressure from 2.5 to 6 % implies an increase of resistivity by one order of magnitude; a stronger variation is present from 10% to 15%.

As stated before, the thickness of the samples is not the same, dividing resistivity by the thickness of the film, sheet resistance (Ω/□) is obtained. The trend of sheet resistance values shown in figure 3.5 is similar to that of resistivity.

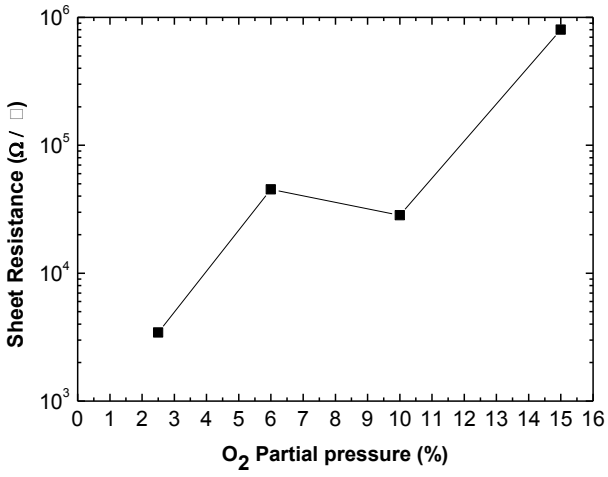

Figure 3.5. Sheet resistance versus O_2 partial pressure.

The presence of higher oxygen content can imply a saturation of vacancies and the reduction of carrier density and by consequence a lower conductivity.

This hypothesis is strengthened by the trend of carrier density versus O_2 partial pressure in figure 3.6. In equation (2.10) carrier density has an inverse proportionality with resistivity, so a better conductor has a higher carrier density, but the presence of a high number of charge carrier implies a higher scattering probability, so a lower mobility. The increase of scattering events is also promoted by the grain boundaries segregation of ionized impurities.

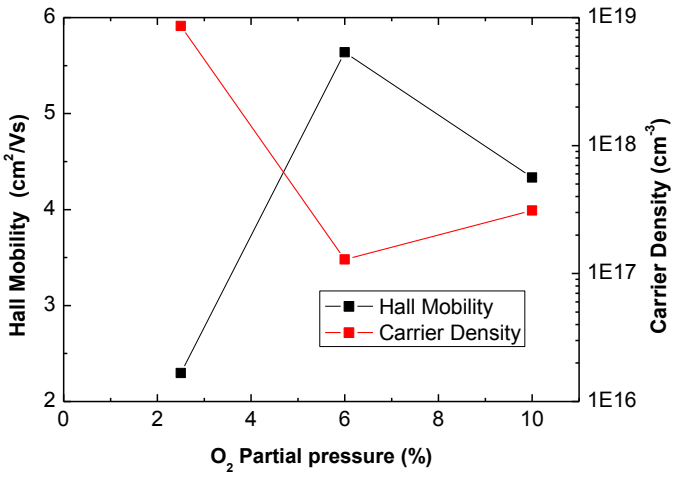

Figure 3.6. Hall mobility and carrier density versus O_2 pressure ratio

Is important to denote that this measurements presents some experimental issues due to the sensibility of data of the magnetic field used to induce Hall effect. Moreover charge transport in nanocrystalline AZO is different from polycrystalline one. In this case electrical transport is affected by grain boundaries scattering and trapping, as already said, therefore the Hall mobility value affected by hopping transport mobility and this can influence Hall measurements.

3.2.3 Cross-plane resistivity measurements

Until now we have considered electrical measurements performed along the in-plane direction, which is a simple measurements carried on also with compact films without any issues. As described in previous sections, these nanostructures present a directional growth which provide an anisotropic material, with different properties depending on the direction considered. In a hypothetical device, for istance the one in figure 3.5, the tree-like nanostructured TCO should be deposited with tree axis perpendicular to the substrate and parallel to the carriers movement inside the solar cell. In this application the the cross-plane direction should be the most important one, so electrical measurement along ortogonal direction with respect of the substrate

plane is fundamental to understand the real ability of carriers transport inside the solar cell.

In order to achieve this purpose, different paths were attempted:

1. One of them consists in fabricating an electrical circuit composed by a substrate of ITO, on which AZO was deposited and a electrical connection made by a indium foil, as drawn in figure 3.7. Considering the ohmic contact, and consequent tension drop, between different conductors negligible compared to the one of AZO, the measured resistance should give an idea aobut the cross-plane resistivity of the film. The connection with indium (melting point of 156°C) is reached melting the foil, into a homemade hoven in vacuum condition, in order to allow the adhesion on AZO and ITO. The result was unsuccessful beacause the foil did not melt and, as consequence, adhesion is not favoured.

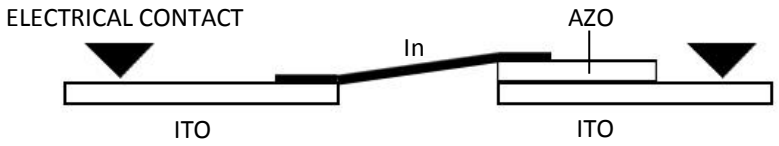

Figure 3.7. Scheme of the first attempt.

2. Another way was to evaporate metallic contact under and on the top of AZO film in order to measure the tree cros-plane electrical transport ability between two electrode (evaporation technique used in this work is described in section 2.1.1). The first problem was the choice of the right material for the electrical contact, in order to achieve an optimal ohmic contact betweem the metal and the semiconductor.

An ohmic contact is defined as a metal-semiconductor contact that has a negligible junction resistance relative to the total resistance of the semiconductor device. An accettable ohmic contact should not significantly perturb the device performance and can supply the required current with a voltage drop that is sufficiently small compared

with the drop across the active region of the device [55]. The parameter must take into account is the work function of both the semiconductor and the metal, which is the minimum thermodynamic work (i.e. energy) needed to remove an electron from a solid to a point in the vacuum immediately outside the solid surface and it is defined for a semiconductor as

$$W_S = \chi + E_C - E_F \tag{3.1}$$

where χ is the electron affinity, E_c is the conduction band energy and E_F is the Fermi energy of the material.

For n-type doping ZnO the work function range is 4.35-5 eV. In order to shape good ohmic contact for AZO, the work function of metal (W_m) should be lower than W_s; that is to say, the W_m should be less than 4.35eV [56].

Considering materials with similar work function, we can find the priority is In, secondly Ti and Al, etc. Based on this theory, researchers are investigating in kinds of material or ways hoping to find out an excellent ohmic contact with ZnO, such as Pt-Ga[57], Ti/Au[58], nonalloyed Al[59], Ti/Al[60], Al/Pt[61], Ta/Au[63], In/Ag, In/Al, and so on [56].

In the choice of the type of material for electrical contact material availability, electrical conducting ability and interaction with porous films were considered and the initial alternatives were Al, Ag, Au. The respective work function are 4.06-4.26, 4.26-4.74 and 5.1-5.47 eV. The decision about the material verged to Al and Au.

As stated in section 2.1.1 an interlayer of chrome were deposited on the substrate to improve the adhesion of gold contact on glass.

The deposition of Al and Ag on porous AZO was performed with a thickness of about 30-40 nm (this is a nominal value, measured by a microbalance during evaporation). The samples were observed with a Scanning Electron Microscope (SEM) in order to detect a surface interface between AZO and metal. SEM images do not give the expected result and an interface between the two materials is not visible, for this reason images are not provided. Probably the porosity of the film enhances the diffusion of these elements.

The attention was focused on the choice of gold as evaporant, in this case a layer was deposited on a porous film (110 Pa in 100% O_2). In figure 3.8 gold particles are visible on the top of the tree-like nanostructured AZO and a layer of about 120 nm were measured.

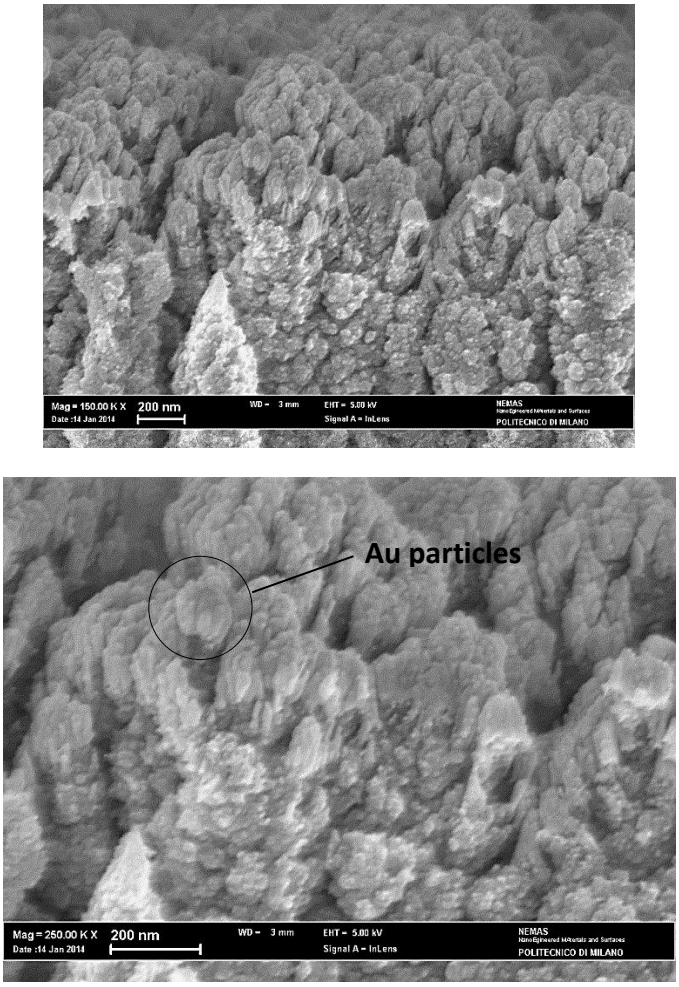

Figure 3.8. SEM immages with different magnification of 120 nm gold layer deposited on porous nanostructured AZO.

The gold layer disposition is similar to the one of graded AZO (figure 1.22) described at the end of the chapter 1, therefore a compact structure on the top of the tree is present.

Finally an optimal configuration, with a Au contact at the bottom of the film and on the top, is achieved. Some measurmement attempts was performed with a two wire configuration, described in section 2.2.1, but a too low resistance was measured, almost comparable to the one of a gold thin film. A possible explanation of this phenomenon is the crush of the film by the pointed electrical contact of the measurement instrument. Unfortunately a tree-like structure forms fragile films, which tends to be easily scratched. In figure 3.9 the impact of the contact on the film is visible.

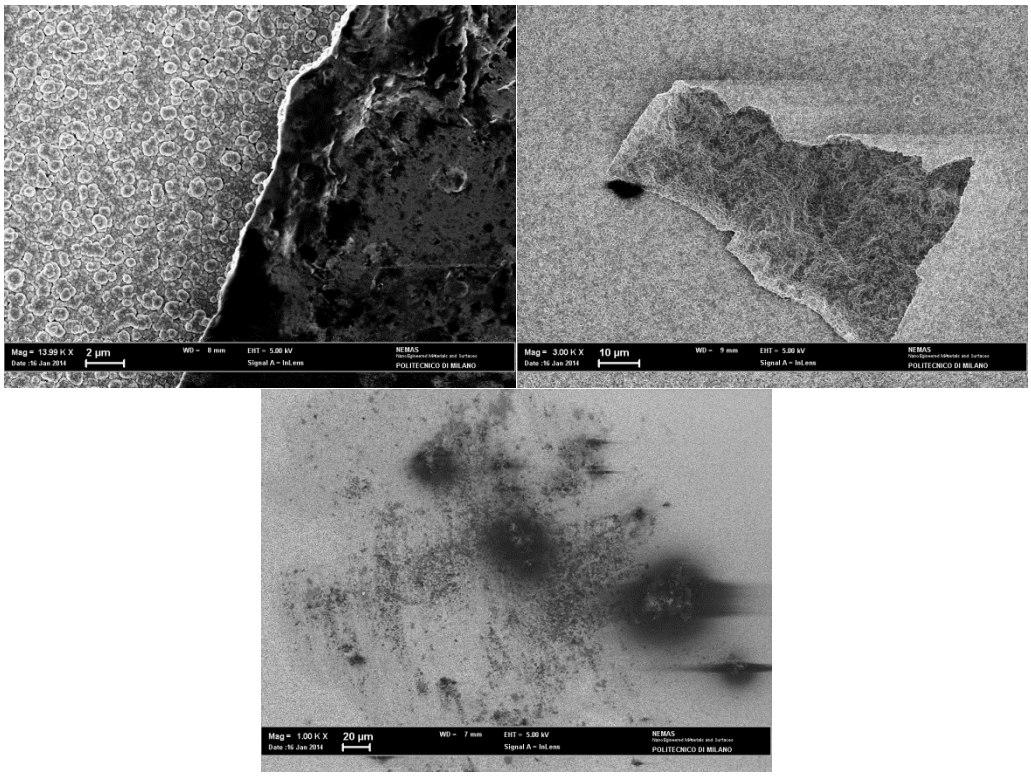

Figure 3.9. On the top images an interface between intact graded AZO and damaged AZO (left) and the pointed contact print (right) are visible. On the bottom a less magnificated picture shows damaged zone.

This research need a deeper investigation, however recent works are in progress and concerns the use of electrical contact with a microtip, which reduces surface contact and possible film damages.

3.2.4 Optical properties

As described in section 2.3, optical measurements were performed. In figure 3.10 transmittance spectra of nanostrctured AZO films deposited with different O_2 partial pressure at a total pressure of 110 Pa inside the vacuum chamber are plotted.

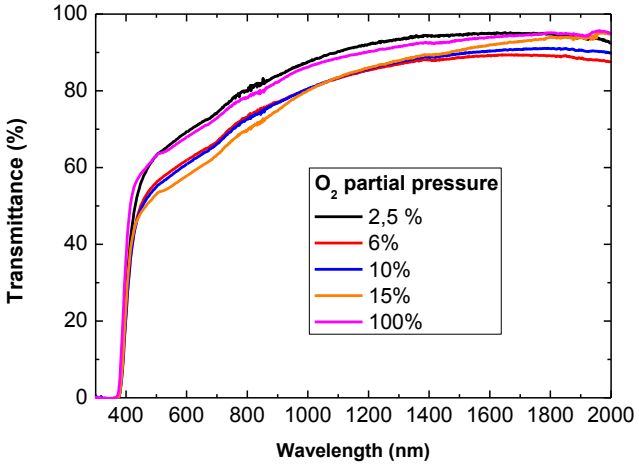

Figure 3.10. Transmittance spectra of hierarchical tree-like structure deposited with different O_2 partial pressure.

A similar optical response of every film is observed, the transmittance profile has a common trend. In the visible range there is the most pronounced difference in transmission, then, at higher wavelength, this difference is attenuated.

Generally these films have the typical behaviour seen in previous work, presented in section 1.4.3 [20,24], with a narrow and steep profile close to the optical band gap; in this range there is the absence of interference fringes, typical of AZO compact thin films, due to the high level of morphological disorder which prevent coherent phenomena. Likewise the surface roughness inhibit the same phenomena at the interface with air.

In the infrared region there is not absorption edge, which would have been present with a higher carrier concentration, like in the case of more compact and conductive films (left graph in figure 1.18).

An important parameter for a TCO is the mean transmittance in the visible range, which is evaluated calculating the average of the percentage of transmitted light between the wavelengths of 400 nm and 700; in figure 3.11 mean transmittance values are present, looking at this graph we can see the sample 2.5% O_2 has almost the highest transmittance in the visible range, but this value is misleading if we do not consider the importance of the thickness of the film, which, as already stated, is not the same for every sample.

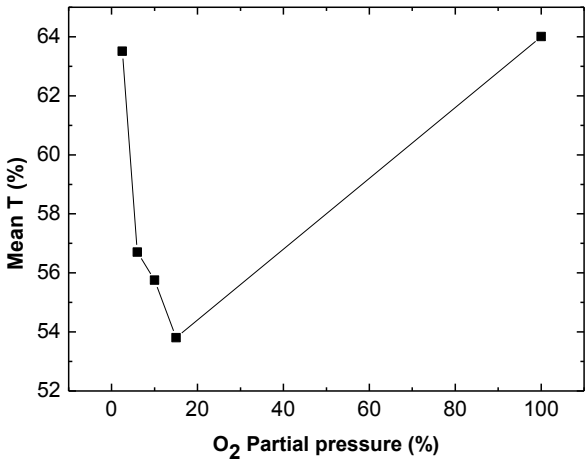

Figure 3.11. Mean transmittance value versus different O_2 partial pressure.

We can neglect the influence of thickness considering the Beer –Lambert law

$$\mathrm{I} = \mathrm{I}_0 \mathrm{e}^{-\alpha \mathrm{x}} \tag{3.2}$$

I is the total radiation intensity, I_0 is the incident radiation, x is the thickness of the sample and α is the attenuation coefficient or absorption coefficient. The ratio between I_0 and I is simply the transmittance. Inverting the equation we can obtain the absorption or attenuation coefficient in function of the thickness and transmittance

$$\alpha = -\frac{1}{x} \ln T \tag{3.3}$$

This formula is useful to obtain the graph in figure 3.12, the lower is the absorption coefficient the more transparent is the material considered, without taking into account the dimension of the film. The contribution of absorption is important and related to transmission by the equation of the conservation of energy

$$a = 1 - t - r \tag{3.4}$$

where a,t and r are the ratio of the light of absorbed, transmitted and reflected intensity. Equation (3.3) assumes that the reflectivity can be neglected, of course because it is very low.

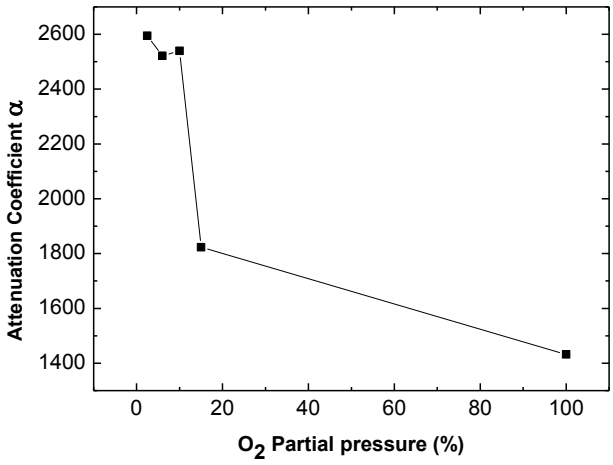

Figure 3.12. Attenuation coefficient versus different O_2 partial pressure.

Therefore we have some changes with respect to the trend of mean transmittance, indeed a decrease of O_2 partial pressure implies a diminishment of transparency. This could be motivated by the presence of more defect states in films with lower O_2 partial pressure films, they are created by the presence of higher concentration of oxygen vacancies.

As stated previously, in addition to integral transmittance measurements, an investigation on light scattering through thin films was performed. The haze factor is the parameter that represents the ability of light scattering by thin films (described in

section 2.3) and it is the ratio of the scattered transmitted light intensity S to the total transmitted intensity T

$$H = \frac{S}{T} \cdot 100 \tag{3.5}$$

The shape of the haze factor curve is shown in figure 3.13, in the lower wavelength region it reaches 100%, then it decreases going to infrared. Hierarchical tree-like structure was chosen to maximize light scattering thank to its open structure and high surface/volume ratio, this ability seems to be independent of the oxygen-argon ratio.

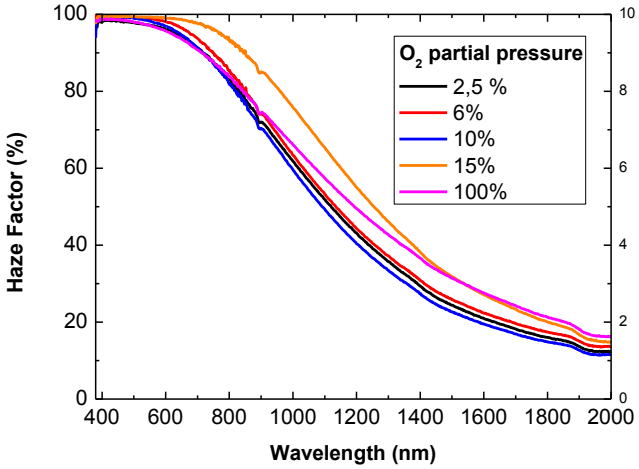

Figure 3.13. Haze factor profile of arboreous AZO films

This supposition is confirmed by figure 3.14, in which the mean haze factor values, evaluated in the visible range, are represented. The variation is between 96 and 99%, which is an optimal level. To apply this kind of material in photovoltaic application, the haze factor should reach the highest possible level, as in this case.

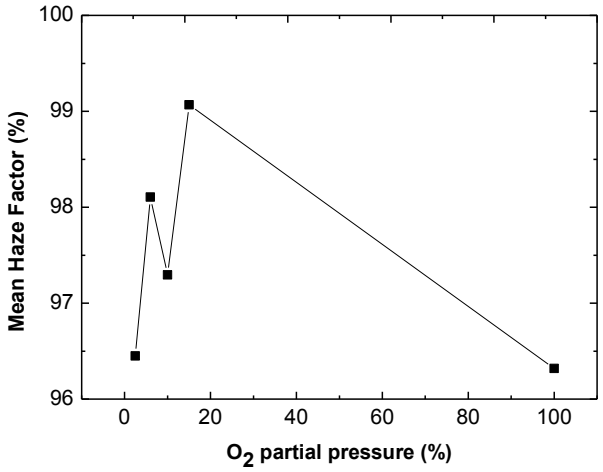

Figure 3.14. Mean haze factor values versus O_2 pressure ratio

3.3 Degradation of functional properties

In this paragraph deterioration of functional properties, especially electrical resistivity, is investigated. As stated in section 1.1.3, the durability of components' materials is fundamental for the life time of solar panels, it strongly affects economic aspects in terms of efficiency. In the previous paragraphs the functional properties described were measured immediately after the deposition, in the case of electrical properties, and few days after, in the case of optical properties.

The monitoring of these features concerns nanostructured AZO samples, deposited at 110 Pa of various Ar:O_2 atmosphere and compact AZO samples, deposited in this work, at 2 Pa in O_2.

Afterwards electrical measurement of 3 years old compact AZO samples (deposited in a previous work) were performed, in order to verify possible variation in conduction ability. A resume of all monitored samples is outlined in table 3.3.

<table>
<tr><th>Deposition Pressure (Pa)</th><th>O_2 Partial pressure</th><th>Structure</th><th>Ageing time</th></tr>
<tr><td rowspan="4">110</td><td>2.5</td><td rowspan="4">Nanoporous</td><td rowspan="5">Monitoring from deposition to about 1 month</td></tr>
<tr><td>6</td></tr>
<tr><td>10</td></tr>
<tr><td>15</td></tr>
<tr><td>2</td><td rowspan="6">100</td><td rowspan="5">Compact</td></tr>
<tr><td>0.01</td><td rowspan="5">About 3 years</td></tr>
<tr><td>1</td></tr>
<tr><td>2</td></tr>
<tr><td>3</td></tr>
<tr><td>10</td></tr>
</table>

Table 3.3. Resume of monitored films.

After deposition and electrical measurements, the samples were contained in plastic case, without the possibility of avoiding interaction with the atmosphere and its degrading agents.

As found in literature, critical factors determines degradation of electrical properties: segregation and diffusion at grain boundaries of H_2O/OH^-, which promotes the increase of a potential barrier and impedes carrier transport [9,51,52]; moreover the absorption and diffusion of different species present into the atmosphere, as moisture, O_2, CO and CO_2, can favour the saturation of oxygen vacancies and reduction of carrier density.

It is important to underline that this work is based on phenomena occurring in ambient conditions, on the contrary literature researches are mostly carried on at controlled and modifiable conditions which permit an acceleration of degradation, for example damp-heat test [52], annealing [53] or high humidity ambient [50].

In this investigation samples with O_2 partial pressure between 2.5 and 15 % were tested, this because over 15% the resistivity reaches too high values, which are not detected by the instrument.

In this experiment a 2 wire configuration, described in section 2.2.1 and by figure 3.3, was selected and resistance values were obtained, with equation 2.7 the film resistivity can be evaluated. The Hall effect measurement were not carried out, because it is strongly affected by nanostructure and related hopping transport phenomena, moreover with 2 wire configuration is not possible to use the configuration shown in figure 2.12.

In figure 3.15 the variation of electrical resistivity of each films in time are shown. It is immediately evident the impossibility of measuring the resistance of 15% film because of its insulating behaviour one day after deposition, the measured resistance was over 200 MΩ.

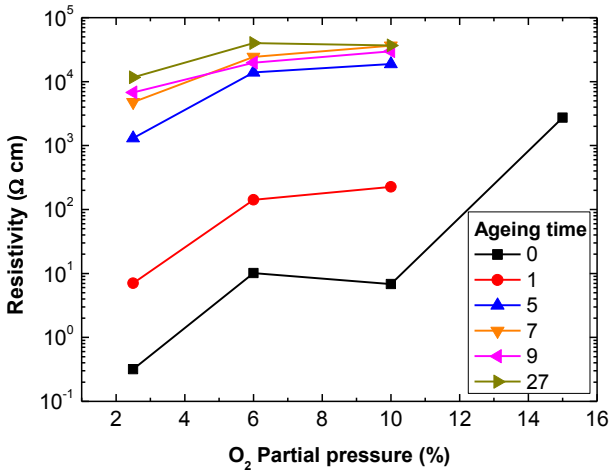

Figure 3.15. Trend of resistivity versus O_2 partial pressure, each colour is related to different ageing time.

In figure 3.16 the trend in time of each samples resistivity is visible. It is important to underline the initial slope of the curve profile, which indicates a quick degradation in the first week after deposition, with the consequent loss of conducting behaviour by nanostructured AZO films, increasing their resistivity of more than 3 order of magnitude, in agreement with O_2 content. After the first interval of time, the parameter reaches a constant value, which depends on oxygen partial pressure, as indicated in table 3.4.

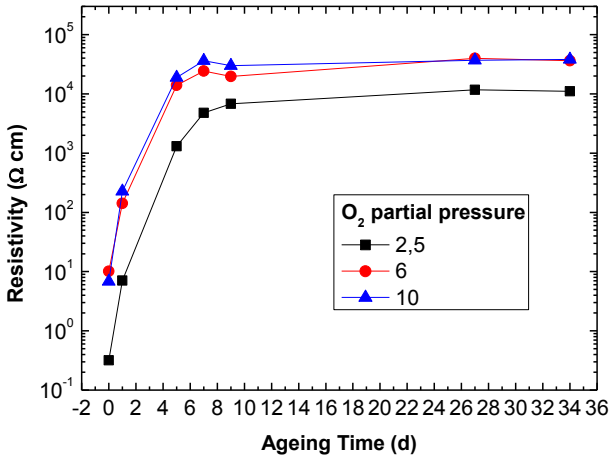

Figure 3.16. Trend of resistivity versus aging time, each colour is related to different O_2 partial pressure (%).

O_2 partial pressure (%)	Resistivity (10^4 Ω cm)	Resistivity after vacuum treatment (10^4 Ω cm)
2.5	1.35	0.6
6	3.64	1.02
10	3.81	1.34

Table 3.4. Electrical resistivity one month after deposition.

To better understand the reason of this phenomenon the aged samples were put inside a vacuum chamber at a pressure of 10^{-3} Pa for about 12 hours, in order to verify if moisture could be a possible cause of deterioration . After this treatment electrical measurements were performed once again to detect an eventual recovery of resistivity. The result was a decrease of almost one third of the resistivity values as indicated in table 3.3. Probably a chemical reaction or oxidation with species diffused into the film occurred [9], therefore this treatment permits to remove the less bonded humidity from the material, because a total recovering of properties was not

observed. Possible chemical reaction are presented by Mirjam Theelen et al. [9], who suggest the chemical formation of zinc hydroxide as follows

$$Zn^{2+} + 2\ OH^{-} \rightarrow Zn(OH)_2 \tag{3.6}$$

A compact film deposited in O_2 atmosphere at a pressure of 2 Pa was taken into account for resistivity variation monitoring. As depicted in figure 3.17 no significant variation was detected in a period of one month, both for electrical resistivity and, as shown in figure 3.18, carrier density and hall mobility.

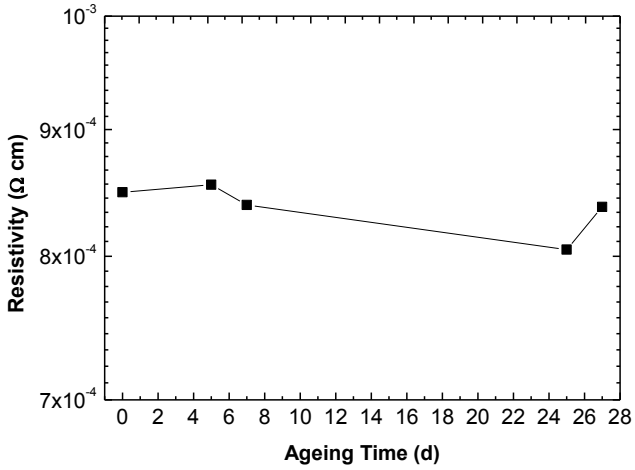

Figure 3.17. Trend of resistivity vs ageing time of a sample deposited at 2 Pa in a O_2 atmosphere.

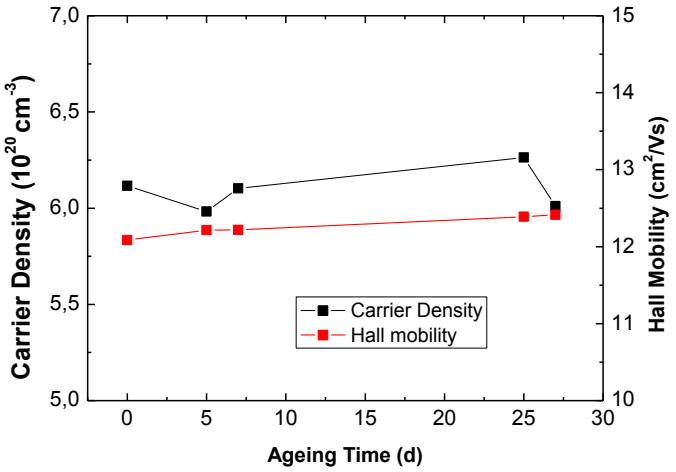

Figure 3.18. Trend of carrier density and hall mobility for a AZO film deposited at a pressure of 2 Pa in a O_2 atmosphere.

As hinted before, some samples characterized in previous thesis work were considered to verify possible degradation process on functional properties. In this case samples were characterized 3 years after deposition, which was carried on at different O_2 total pressure. These samples have a compact columnar structure and do not present significant variation of resistivity values, as shown in figure 3.19.

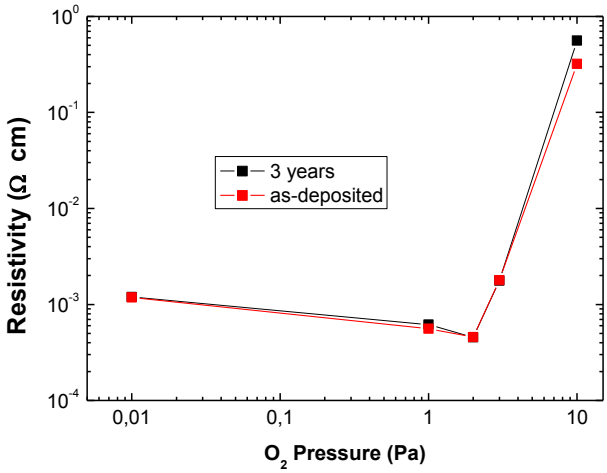

Figure 3.19. Profile of resistivity variation versus O_2 pressure of samples as deposited and 3 years after deposition.

This confirms that compact samples does not undergo degradation of electrical resistivity and maintain their conducing behaviour. Instead carrier density and hall mobility present some variation as plotted in figure 3.20 and 3.21. Except for samples deposited at a pressure of 1 and 2 Pa, carrier density of 0.01 Pa decreases of about an half, 2 Pa more than 2 times and 10 Pa of one order of magnitude. The measurements of 3 and 10 Pa samples are affected by the increase of porosity and the structure begin to be similar to tree-like open structure. However the increase of carrier density was not predictable and needs a deeper investigation to be explained.

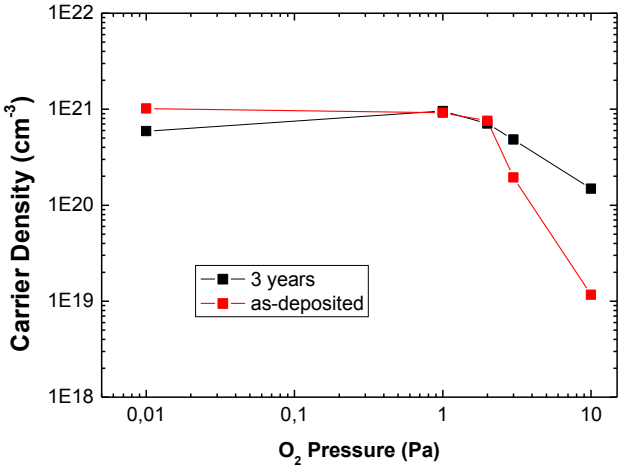

Figure 3.20. Trend of carrier density variation versus O_2 pressure of samples as deposited and 3 years after deposition.

The trend of Hall mobility is similar, because 1 and 2 Pa is unchanged, while 0.01 increases of one half, 3 Pa decrease with the same ratio of the sample before, the 10 Pa hall mobility lost one order of magnitude.

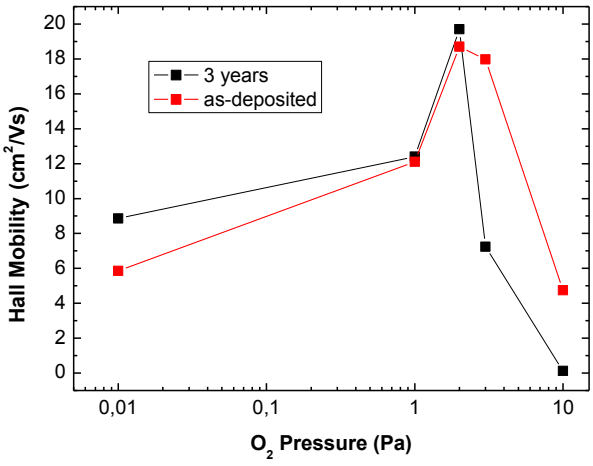

Figure 3.21. Trend of Hall mobility variation versus O_2 pressure of samples as deposited and 3 years after deposition.

Probably, these differences can be explained with the help of the analysis presented in section 1.4, in which is shown the variation of the domain size versus deposition pressure (figure 1.15). Lower dimension of the grains implies a higher number of grain boundaries, which means a higher influence of them on carrier density and Hall mobility. A possible diffusion of OH^- at grain boundaries can decrease Hall mobility, increasing potential barrier, which impedes normal transport phenomena. This implies a higher concentration of trapping site.

From this set, a samples deposited at 2 Pa, with a thickness of 1 µm, was chosen for optical transmittance measurement. The graph in figure 3.22 points out unchanged optical transmittance in the visible range also 3 years after deposition. In the infrared range, over a wavelength of 700 nm, a small divergence between the two curves is present. This could be associated with the diffusion of moisture and difference species inside the film. The higher absorption can be correlated to the presence of higher traps concentration, as stated before, which reduce the level of transparency in the infrared region. However, the weight of this aspect is reduced by the compactness of the film, which makes the molecules diffusion difficult, this aspect is described in more

details in section 3.4, where a correlation between different functional properties is carried out.

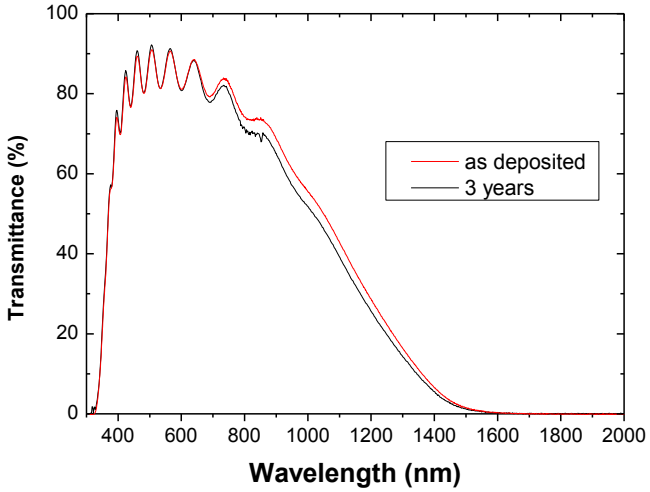

Figure 3.22. Transmittance spectra comparison between a 2 Pa sample with different ageing time.

3.4 Discussion

In this section a correlation analysis between functional properties, which have been presented and discussed in previous paragraphs, is provided.

As seen before, O_2 partial pressure strongly affects electrical properties of AZO nanoporous thin films. A genenal trend of electrical resistivity is present, increasing O_2 content implies an increment of resistivity and, of course, sheet resistance. Considering also the resistivity value of the 100% O_2 sample measured in previous work, this property spans across 6-7 order of magnitude.

The main reason of this variation is the saturation of oxygen vacancies by oxygen atoms present in the deposition atmosphere. A lower partial pressure means lower O_2 content inside the film, this implies higher number of holes which enhance film conductivity. So defects of Al, which is the dopant, and oxygen are the most important factor which affect electrical properties, this is confirmed by some annealing treatments carry out in vacuum or inert atmoshpere, not performed I this work, in

which the desorption of O is favoured; this implies a reduction of resistivity of some order of magnitude.

Morphology can be just a secondary aspects for the influence of transport properties, but we cannot have experimental confirmations.

In the thesis work of Gondoni P. [24] an analysis of scattering mechanisms in relation with Hall mobility and total deposition pressure is provided. At higher pressure deposition, as in our case, the most predominant scattering phenomenon is due to the interaction with grain boundaries. So that explains why there is a reduction of conductivity in correspondence of an increase of number of grain boundaries and reduction of number of oxygen vacancies. Of course this influences the trend of Hall mobility, which increases with a rising of the O_2 content, and of carrier density, which decrease with the saturation of oxygen vacancies and the formation of zinc hydroxide.

The films morphology influences also cross-plane measurements attempted in this work. The evaporation of metal contact on AZO is difficult because of the porosity and roughness of this nanostructured films. The higher the porosoty the higher is the atom diffusion inside the film, therefore the obtaining of a homogenous metal film on AZO surface is impossible because the high surface roughness.

A future work should be focused on the evaporation of metal contacts on a graded AZO film, on the top of which it has a compact layer is deposited at 2 Pa (as seen in figure 1.22). The measure should take into account that the resistivity of compact layer is sufficient lower than the one of the porous layer at the bottom, so it can be neglected. The resistance measured is of the porous film. Unfortunately the problem of film damageability must be solved.

A possible solution is provided by Università di Modena and Reggio Emilia, at Department of Science Physics, supervised by Dr V. De Renzi and Dr G. Gazzadi, the measure was performed by depositing AZO layers on commercially available conducting ITO substrates (R_S = 10 Ω/□) and acquiring I/V curves with Pt-coated micromanipulators.

With this procedure it is difficult to extract an accurate resistivity value due to uncertainty about the right number of nanotrees in the bundle and about the path travelled by electrical current. For the measurements, the section of the trees column corresponds to the probe diameter of 10 μm^2, and the thickness is equal to 1 µm, as in the case of two wire configuration, the application of Ohm's law indicates that the order of magnitude of in-plane and cross-plane electrical resistivity are compatible.
The orders of magnitude of measured cross-plane resistances were: 10^4 Ω at 6% O_2, 10^5 Ω at 10% O_2 and 10^{10} Ω at 100% O_2.
The in-plane resistances of porous samples, measured in this work one week after deposition with a two wire configuration, are: $2.4 \cdot 10^7$ Ω at 2.5% O_2, $8.5 \cdot 10^7$ Ω at 6% O_2 and $1.7 \cdot 10^8$ Ω at 10% O_2. A comparison between the two experimental results can be done just for 6 and 10%: a difference of 3 order of magnitude is present. This could be explained considering the lower continuity present along the in-plain direction, because the material growth occurred along the vertical direction, as stated before.

The low conductivity of porous films is confirmed by the profile of transmittance curves in figure 3.8. The absence of absorption phenomena at higher wavelenght, into the infrared range, is a consequence of shortage of free electrons. The transmittance depends strongly by the thickness, so absorption coefficient is evaluated by equation (3.3), to extimate thin film optical absorption regardless of its thickness. The coefficient decreases with an enhancement of the O_2 partial pressure, the oxygen vacancies saturation level affects also the film transparency. This means that increasing O_2 partial pressure, also optical transmission enhances.
As is shown in figure 3.12 the light scattering ability of AZO nanostructured, with a film thickness of about 2 µm, is independent of oxygen content; a value near the unity is reached for all the films considered, this underlines the good ability of light scattering of hierarchical tree-like nanostructures.

The investigation of ageing degradation concerns both porous nanostructured and compact columnar thin films. Of course the main feature that influences this

phenomenon is film porosity. The diffusion of moisture and other chemical species present into the atmosphere is facilitated by tree-like structure regardless of O_2 partial pressure, which is not the dominant factor for this physical phenomenon, but it affects the as deposited value of resistivity and the constant value reached after the first interval of time after PLD process. The resistivity of porous films reaches a sort of saturation level about one week after PLD process, with an increase of about 3 orders of magnitude for each film considered. Contrariwise compact films do not suffer ageing until the deposition pressure considered reaches 10 Pa, at which a more porous columnar structure is observed, as depicted in figure 1.14. In this case resistivity almost doubles its value and also Hall mobility and carrier density vary. The deterioration of electrical properties are related to border grain scattering and segregation of chemical species adsorbed on the surface that generate trapping sites for charge carrier; also possible oxidation occurred after deposition process. The low grain size and presence of mesopores in nanostructured AZO contribute strongly to the degradation process.

As confirmed by data and resulting conjectures, the main issues in engineering a TCO and a chosen nanostructures is not the achievement of optimal functional properties, but it is the prevention of their deterioration.

Chapter 4

Conclusions, perspectives and future developements

In this thesis work hierarchical tree-like nanostructured AZO thin films were deposited by Pulsed Laser Deposition at room temperature, with constant vacuum chamber deposition pressure of 110 Pa composed by different $Ar:O_2$ mixtures, in order to investigate the effects of oxygen stoichiometry on AZO functional properties, which is interesting for photovoltaic applications.

AZO thin films is used as material for Transparent Conducting Oxide (TCO), which must have high optical transparency and high electrical conductivity as main features. Recent works verge to materials that maximize light scattering and a possible solution is the use of hierarchical nanostructures with wide surface/volume ratio and open structure. In this context all this properties were studied and correlated with morphological and structural analysis. The latter investigation was performed by means of Scanning Electron Microscope, with which also thickness measurements were carried on. At O_2 partial pressure lower than 15%, the preferential growth direction of tree bundles is almost lost together with the compactness of aggregates. Thickness measurements reveal different film thickness, this is probably due to the variation of porosity changing O_2 partial and to possible chemical reactions with oxygen occur during deposition.

The effect of oxygen content on optical properties was performed with a UV-vis-NIR spectrophotometer, the data obtained allow to observe direct and scattered transmittance versus wavelenght. Moreover the attenuation coefficient was obtained, neglecting reflecting phenomena, from Beer-Lambert law, with which thickness variation effects are taken into account; its significant decrease was identified with the

increase of O_2 partial pressure, this suggests higher transparency for higher O_2 content. Haze factor is not sensitive to oxygen partial pressure, and in the visible range it reaches a value almost near 100%, underlining a good light scattering ability of forest-like nanostructured layers.

Electrical transport properties were measured following Van der Pauw configuration and procedure. Oxygen stoichiometry strongly affects electrical properties like resistivity, carrier density and Hall mobility. An increase of O content reduces electrical conductivity, from 2.5 to 100% of O_2 partial pressure there is an increment in resistivity of 5-6 order of magnitude, with a minimum of $3{,}17 \cdot 10^{-1}$ Ω cm at 2.5% O_2. The reduction of oxygen content is the right direction to fabricate nanoporous AZO thin films with improved electrical properties, however the resistivity value of compact AZO thin films, of about $4 \cdot 10^{-4}$ Ω cm, is far away.

In this work some attempts to perform cross-plane measurement were performed. The main procedure consisted in the deposition of gold contacts at the bottom and on the top of porous films in order to measure the resistance between contacts; the roughness and porosity of AZO did not alow to obtain a homogeneous gold layer, moreover a higher mechanical resistance of the film prevents the detection of the current along the bundle of nanotree.

The parallel work about cross-plane electrical resistivity measurement performed by Università di Modena and Reggio Emilia, allows a comparison with in plane electrical transport. A higher carrier transport ability is measured along the vertical direction, parallel to tree axis; an optimization of measurement could give us a better understanding about the physics of this phenomenon inside a hierarchical nanostrtucture.

Another important aim of this thesis work was a qualitative discussion about the deterioration of functional properties of AZO films by monitoring the deterioration of electrical resistivity upon ageing. In this experimental phase also AZO compact films deposited in O_2 atmosphere with different pressures (see table 3.2) were considered.

A different degradation of resistance behaviour, depending mostly on porosity, was observed:

- a quick deterioration of electrical resistivity was detected for nanostructured AZO thin films of about 4 order of magnitude, a stable value is reached after a little bit more than one week, the final value depends on O_2 partial pressure as stated before;
- a good stability is shown by compact films, deposited in O_2 atmosphere, till a deposition pressure of 2 Pa, in which no electrical properties variation was detected both in the first month and 3 years after deposition;
- optical transmittance measurement was performed on 2 Pa sample, in which just a little variation of transparency is seen (3% of transmittance) in the infrared region.

The results obtained from the monitoring of ageing degradation of electrical resistivity of nanostructured AZO thin films, reveal an importante issue in the choice of this material and related nanostructure for real applications. The properties deterioration requires a protection coating of an hypothetical TCO and the interaction with atmosphere must be prevented in order to avoid the diffusion of moisture and other detrimental chemical species inside the film, which can cause chemical reaction and segregation at grain boudaries.

Without considering this physical phenomenon, the most performant forest-like nanostructured Aluminum doped Zinc Oxide is the 2.5% O_2. The maximum reduction of oxygen content, preserving optimal optical properties, is the right choice to the best improvement of electrical conduction.

In an immediate future an investigation of the effects of thermal treatments, as annealing, in vacuum and in inert atmosphere should allow to explain both the contributions of morphology and stoichiometry in determining electrical properties. Furthermore a study of the recovery of electrical properties after degradation with the use of thermal treatments should be considered to better understand

phenomenological aspects of ageing process on AZO. In this background the monitoring of optical properties after deposition should be carried out. A different way to study the physics of these films should be performed controlling film growth by changing the temperature of the substract during deposition process, in order to observed a possible variation of the material growth mechanisms and related properties. Finally the development of new methods to perform cross-plane measurements should be carried on to better understand vertical electrical transport ability.

References

[1] Minami, T. Semicond. Sci. Tech. 20, 35_44 (2005).

[2] Ashcroft, N. W. and Mermin, D. N. Solid State Physics, Thomson Learning, Toronto, January (1976)

[3] Pasquarelli, R.M., Ginley, D.S. and O'Hayre, R. Chem. Soc. Rev., 2011, 40, 5406–5441

[4] Hosono H., Paine D.C., Ginley D.S. (eds.) Handbook of Transparent Conductors, Springer (2010)

[5] Coutts, T. J. and Young, D. L. MRS Bulletin 25, 58-65 (2000).

[6] Grundmann, M. *The Physics of Semiconductors*, 2nd ed., Springer (2010)

[7] Roshidah Rusdi, Azilah Abd Rahman, Nor Sabirin Mohamed, Norashikin Kamarudin, Norlida Kamarulzaman. Powder Technology 210 (2011) , 18–22.

[8] Fan, J. and Goodenough, J. Journal of Applied Physics 48(8), 3524_3531, (1977).

[9] Mirjam Theelen, Twan Boumans, Felix Stegeman, Fallon Colberts, Andrea Illiberi, Jurgen van Berkum, Nicolas Barreau, Zeger Vroona, Miro Zemanb. Thin Solid Films 550 (2014) 530–540

[10] T. K. Subramanyam, B. Srinivasulo Niudu, S. Uthanna. Cryst. Res. Technol., 35, 2000, 10, 1193–1202

[11] Exarhos, G. J. and Zhou, X.-D. Thin Solid Films 515(18), 7025-7052, (2007).

[12] Bellingham, J., Phillips, W., and Adkins, C. Journal of Materials Sciences Letters 11, 263_265 (1992).

[13] Fortunato, E., Ginley, D., Hosono, H., and Paine, D. C. MRS Bulletin 32, 242_247 (2007).

[14] Ellmer, K. Thin Solid Films 496, 104 _ 111 (2006).

[15] Chang, S.-Y., H. Y.-C. H. Y.-C. Surface and Coatings Technology 202(22-23), 5416_5420 (2008). cited By (since 1996) 10.

[16] Ellmer, K., Klein, A., Rech, B. Transparent Conductive Zinc Oxide: Basics and Applications in Thin Film Solar Cells, Springer (2010)

[17]Özgür, U., Alivov, Y. I., Liu, C., Teke, A., Reshchikov, M. A., DoÄ.an, S., and Avrutin, V. Journal of Applied Physics 98, 1_103 (2005).

[18]Venkatachalam, S., Iida, Y., and Kanno, Y. Superlattices and Microstructures 44, 127_135 (2008).

[19]Agashe, C., Kluth, O., Hüpkes, J., Zastrow, U., Rech, B., and Wuttig, M. Journal of Applied Physics 95(4), 1911_1917 (2004).

[20]P. Gondoni, M. Ghidelli, F. Di Fonzo, M. Carminati, V. Russo, A. Li Bassi and C. S. Casari, Nanotechnology 23 (2012)

[21]Gondoni P, Ghidelli M, Di Fonzo F, Russo V, Bruno P, Mart´ı-Rujas J, Bottani C E, Li Bassi A and Casari C S 2012 Thin Solid Films 520 4707

[22]B. Dong, H. Hu, G. Fang, X. Zhao, D. Zheng, Y. Sun, J. Appl. Phys. 103 (2008) 73711

[23]P. Gondoni, P. Mazzolini, V. Russo, A. Petrozza, A.K. Srivastava, A. Li Bassi and C.S. Casari. “Enhancing light harvesting by a hierarchical functionally graded transparent conducting Al-doped ZnO structure” . Submitted by Solar Energy Materials & Solar Cells.

[24]P. Gondoni, Proprietà ottiche e di transporto elettrico di film di ZnO drogato Al per applicazioni fotovoltaiche, thesis work, Politecnico di Milano, 2010 110

[25]Jo, Y.D., Hui, K.N., Hui, K.S. , Cho, Y.R., Kim, K.H. Materials Research Bulletin, Volume 51, March 2014, Pages 345-350

[26]Ben Ayadi, Z. , Mahdhi, H., Djessas, K., Gauffier, J.L., El Mir, L., Alaya, S. Thin Solid Film, 2013

[27]Nehmann, J.B. , Ehrmann, N., Reineke-Koch, R., Bahnemann, D.W. Thin Solid Film, 2014

[28]Socol, G. , Socol, M.b, Stefan, N., Axente, E., Popescu-Pelin, G., Craciun, D., Duta, L., Mihailescu, C.N., Mihailescu, I.N., Stanculescu, A., Visan, D., Sava, V., Galca, A.C., Luculescu, C.R., Craciun, V. Applied Surface Science Volume 260, 1 November 2012, Pages 42-46

[29]An, H.-R.a, Baek, S.-H.b, Park, I.-K.ac , Ahn, H.-J.a. Korean Journal of Materials Research Volume 23, Issue 8, 2013, Pages 469-475

[30]Carlo S Casari and Andrea Li Bassi. Pulsed Laser Deposition of Nanostructured Oxides: from Clusters to Functional Films. In William T Arkin, editor, Advances in Lasers and Optics Research, volume 7, chapter 2, pages 65100. Nova Science Publishers, Inc, Hauppage, NY, 2012.

[31]Chrisey D. B., Hubler G. Eds. Pulsed Laser Deposition of Thin Films. Wiley & Sons: New York, 1994.

[32]Eason R. Ed. Pulsed Laser Deposition of Thin Films. Wiley: Hoboken, NJ, 2007.

[33]Willmott P. R., Huber J. R. Reviews of Modern Physics, 2000, 72, 315.

[34]Itina T. E., Marine W., Autric M. Applied Surface Science, 2000, 154-155, 60-65.

[35]Arnold N., Gruber J., Heitz J. Applied Physics A, 1999, 69, S87-S93.

[36]Chen K. R., Leboeuf J. N., Wood R. F., Geohegan D. B., Donato J. M., Liu C. L., Puretzky A. A. Applied Surface Science, 1996, 45, 96-98.

[37]Amoruso S., Sambri A., Vitiello M., Wang X. Applied Surface Science, 2006, 252, 4712-4716.

[38]Van der Pauw, L. J. Philips Research Reports 13(1), 1-9 (1958).

[39]C. Kelley, Solving Nonlinear Equations with Newton's Method, Society for Industrial and Applied Mathematics, Philadelphia, (2003)

[40]Thurber, W. R. http://www.nist.gov/pml/semiconductor/hall.cfm, (National Institute of Standards and Technology).

[41]Ohring, M. Materials science of thin films, 2nd ed., Accademic press, 2002.

[42]Mattox, D.M. Handbook of physical vapour deposition, 2nd ed., William Andrew, 2010

[43]R.H. Lyddane, R.G. Sachs, E. Teller .Phys. Rev., 59 (1941), p. 673

[44]Wooten, F. Optical properties in solids. Academic Press, (1972).

[45]Alan E. Delahoy and Sheyu Guo. Chapter 17 : Transparent Conducting Oxides for Photovoltaics, in Handbook of Photovoltaic Science and Engineering, John Wiley & Sons Inc; 2 edizione (15 marzo 2011).

[46]Igasaki Y, Saito H, J. Appl. Phys. 70, 3613 (1991).

[47]Koida T, Fujiwara H, Kondo M, Sol. Energy Mater. Sol. Cells 93, 851 (2008).

[48]Makino T, Segawa Y, Tsukazaki A, Ohtomo A and Kawasaki M 2006 Phys. Status Solidi c 3 956

[49]Kim, H., Horwitz, J. S., Qadri, S. B., and Chrisey, D. B. Thin Solid Films 421, 107111 (2002).

[50]Yen-Shuo Liu, Chih-Yi Hsieh, Yen-Ju Wu, Yu-Shan Wei, Po-Ming Lee, Hsiu-Ming Hsieh, Cheng-Yi Liu. Applied Surface Science, 282, 2013, 32– 37.

[51]Jérôme Steinhauser, Stefan Meyer, Marlène Schwab, Sylvie Faÿ, Christophe Ballif, U. Kroll, D. Borrello. Thin Solid Films, 520, 2011, 558–562.

[52]Jae Ik Kim, Woojin Lee, Taehyun Hwang, Jongmin Kim, Seung-YoonLee a, Suji Kang, Hongsik Choi, Saeromi Hong, Helen Hejin Park, Taeho Moon, Byungwoo Park. Solar Energy Materials & Solar Cells, 122, 2014, 282–286.

[53]Deok-Kyu Kim, Hong Bae Kim. Current Applied Physics, 13, 2013, 2001-2004.

[54]Sze, S.M. Physics of Semiconductor Devices. John Wiley & Sons, 1981.

[55]Yao Lv, Lixi Wan. Recent Progress of Ohmic Contact on ZnO. (modificare reference)

[56]A. Inumpudi, A.A. Iliadis, S. Krishnamoorthy, et al. Solid-State Electronics, Vol.46 (2002),pp.1665-1668.

[57]Han-Ki Kim, Sang-Heon Han, and Tae-Yeon Seong. Applied Physics Letters, Vol.77, No.11 (2000), pp.1647-1649.

[58]H. Sheng, N.W. Emanetoglu, S.Muthukumar, et al. Journal of Electronic Materials, Vol.31, No.7 (2002),pp.811-814.

[59]Soo Young Kim, Ho Won Jang, Jong Kyu Kim, et al. Journal of Electronic Materials, Vol.31,No.8 (2002),pp.868-871.

[60]Han-Ki Kim, Kyoung-Kook Kim, Seong-Ju Park, et al. Journal Of Applied Physics, Vol.94,No.6 (2003),pp.4225-4227.

[61]H. Sheng, N.W. Emanetoglu, S.Muthukumar, et al. Journal of Electronic Materials, Vol.32, No.9 (2003) ,pp.935-938.

[62]Soo Young Kim, Ho Won Jang, Jong Kyu Kim, et al. Journal of Electronic Materials, Vol.31,No.8 (2002),pp.868-871.